frontiers | Frontiers in Earth Science

TYPE Original Research
PUBLISHED 16 October 2023
DOI 10.3389/feart.2023.1270053

OPEN ACCESS

EDITED BY
Chang Zhang,
Chinese Academy of Sciences (CAS),
China

REVIEWED BY
Gaoxue Yang,
Chang'an University, China
Xiaohan Gong,
China University of Geosciences, China

*CORRESPONDENCE
Anas A. Karimov,
anas@igc.irk.ru

RECEIVED 31 July 2023
ACCEPTED 27 September 2023
PUBLISHED 16 October 2023

CITATION
Gornova MA, Belyaev VA, Karimov AA, Skuzovatov SY, Karmanov NS, Medvedev AY and Bryanskiy NV (2023), Supra-subduction melt modification of the fossil subcontinental lithospheric mantle: insights from ultra-depleted Khara-Nur ophiolitic peridotites (Eastern Sayan, central Asian orogenic belt). *Front. Earth Sci.* 11:1270053. doi: 10.3389/feart.2023.1270053

Supra-subduction melt modification of the fossil subcontinental lithospheric mantle: insights from ultra-depleted Khara-Nur ophiolitic peridotites (Eastern Sayan, central Asian orogenic belt)

Marina A. Gornova[1], Vasiliy A. Belyaev[1], Anas A. Karimov[1,2]*, Sergei Yu. Skuzovatov[1], Nikolay S. Karmanov[3], Alexander Ya. Medvedev[1] and Nikolay V. Bryanskiy[1,2]

[1]Vinogradov Institute of Geochemistry, Siberian Branch of Russian Academy of Sciences, Irkutsk, Russia, [2]Institute of the Earth's Crust, Siberian Branch of Russian Academy of Sciences, Irkutsk, Russia, [3]Sobolev Institute of Geology and Mineralogy, Siberian Branch of Russian Academy of Sciences, Novosibirsk, Russia

Mantle peridotites from the Mesoproterozoic forearc-type ophiolites in the Eastern Sayan range (Eastern Siberia) provide insights into the nature and formation processes of the supra-subduction mantle. The peridotites are represented by porphyroclastic harzburgites and dunites. The harzburgites have strongly refractory compositions recorded in high Mg# olivine (0.912-0.927) and orthopyroxene (0.916-0.935), high Cr# spinel (0.45-0.66), low Al_2O_3 and Cr_2O_3 abundances in orthopyroxene, the lack of residual clinopyroxene, low HREE abundances in orthopyroxene, clinopyroxene and whole-rocks. Some rocks are relatively enriched in SiO_2, which is a common feature of supra-subduction (arc and forearc) peridotites and suggests hydrous melting, whereas the rest resemble the chemistry of residues from anhydrous melting of depleted mantle (DM). The whole-rock Al_2O_3 and Cr-spinel compositions reflect high degrees of partial melting, which initiated in the garnet facies. The Khara-Nur peridotites experienced modification by high-Mg, low-Ti hydrous (boninitic or tholeiitic) arc melts, which crystallized newly-formed minerals (clinopyroxene, Cr-spinel, olivine) in harzburgites. The trace-element composition of clinopyroxene (Yb_N = 0.5-1.0, La/Yb_N = 0.05-0.5) resembles that of clinopyroxene from the forearc peridotites and reflects low melt/rock ratio. In dunites, melt percolation resulted in growth of Cr-spinel hosting multiphase inclusions (olivine + clinopyroxene + orthopyroxene + amphibole + phlogopite). Clinopyroxenes from Cr-spinel-hosted inclusions exhibit considerable variations in trace element composition due to heterogeneity of parental melts. Remarkably low $Fe^{3+}/\sum Fe$ ratios (0.02-0.12) of Cr-spinels in both harzburgites and dunites are uncommon in SSZ mantle rocks and cannot be explained in terms of the supra-subduction processes, such as partial melting and melt percolation. The whole-rock and mineral compositions of Khara-Nur peridotites, along with previously reported Paleo- to Mesoproterozoic Re-Os model ages, suggest an affinity to ultra-depleted Proterozoic subcontinental

lithospheric mantle (SCLM). Overall, the Khara-Nur mantle rocks most likely represent a block of SCLM which underwent melt interaction in a supra-subduction tectonic setting that yielded boninitic and tholeiitic melts comprising now the crustal part of Eastern Sayan ophiolites.

KEYWORDS

supra-subduction ophiolites, ophiolitic peridotites, redox state, SCLM, mantle wedge, melt-rock reaction

1 Introduction

Subduction zones are the most important sites of net crustal growth and chemical recycling. Over a few decades, the supra-subduction zone (SSZ) mantle has been an object of intense studies based on arc peridotite xenoliths in volcanic rocks (Bénard and Ionov, 2013; Bénard et al., 2017; 2018; Tollan et al., 2017), forearc peridotites from the modern oceans (Parkinson and Pearce, 1998; Pearce et al., 2000; Birner et al., 2017), and mantle sections of SSZ ophiolites (e.g., Zhou et al., 2021; Khedr et al., 2022). More specifically, in case of the fore-arc mantle, the highly depleted nature of harzburgites from all these settings, their similar SiO_2 enrichment, lack of residual clinopyroxene, the presence of high-Mg silicates and high-Cr spinels as well as low whole-rock Al_2O_3 and HREE contents (e.g., Song et al., 2009; Bénard et al., 2017; Zhou et al., 2021) are considered to result from high degrees of hydrous melting of the mantle modified by slab-derived fluids/melts (Bénard et al., 2017). Nonetheless, variable melting degrees, melt/fluid metasomatism and multi-stage formation of suprasubduction wedges are capable of generating significant compositional and redox heterogeneity of SSZ mantle (e.g., Parkinson and Pearce, 1998; Pearce et al., 2000; Arai and Ishimaru, 2007).

Partial melting of the depleted mantle above subduction zones is governed mainly by fluxes of hydrous fluids or H_2O-rich melts from a subducted slab (Grove et al., 2006), which is a generally-applied model for common types of subduction-related magmas including arc basalts and andesites. In case of the forearcs, flux melting triggered by slab-derived fluids and melts (e.g., Pagé et al., 2008) and adiabatic decompression melting of asthenosphere during subduction initiation and fast slab roll-back (Reagan et al., 2010; Dilek and Furnes, 2011) produce a range of melt compositions varying from forearc basalts (FAB) compositionally similar to mid-ocean ridge basalts (MORB) and back-arc basin basalts (BABB), to island arc tholeites (IAT) and boninites, and their complementary, variably depleted mantle peridotites with geochemical characteristics of abyssal and forearc peridotites (e.g., Whattam et al., 2011). The original chemical signatures of variably depleted SSZ mantle are often hampered by abundant melt-peridotite interaction (Bryant et al., 2007; Batanova et al., 2011; Zhou et al., 2021). The process is recorded in specific microstructural features, the appearance of newly-formed minerals and modification of modal and chemical composition of harzburgites to produce dunites and pyroxenites (Borghini et al., 2013; Su et al., 2016; Rogkala et al., 2017; Le Roux and Liang, 2019; Karimov et al., 2020; Zhou et al., 2021), amphibole-phlogopite veins (Bryant et al., 2007) and clinopyroxene-glass reaction patches (Tollan et al., 2017). In some cases, this melt interaction is recorded in Cr-spinel-hosted mineral and melt inclusions, which are relatively rare and were documented in dunites from modern forearcs (Morishita et al., 2011) and ophiolites (Zhou et al., 2021). Another important stage of SSZ mantle formation is cooling and mineral re-equilibration below the wet solidus combined with decompression uplift to shallow mantle depths, resulted in lower equilibrium temperatures in SSZ peridotites compared to abyssal peridotites (Sun and Liang, 2014; Dygert and Liang, 2015; Tollan et al., 2017; Liang et al., 2021).

The fluid-dominated metasomatism is also widespread in supra-subduction mantle (Widom et al., 2003; Arai and Ishimaru, 2007; Bénard and Ionov, 2013) and apparently could operate both before (Tollan et al., 2017) and after the stage of peridotite-melt interaction (Zhou et al., 2021). Fluid-modified metaperidotites of mantle wedge, which exhibit the assemblages of hydrous minerals (i.e., tremolite, chlorite, antigorite) (e.g., Evans and Frost, 2021; Xie et al., 2021; Dandar et al., 2023), are important indicators of cooling and compression to LT-HP conditions (Khedr and Arai, 2010; 2012), and show systematic enrichment in fluid-mobile elements (Scambelluri et al., 2001; Hattori and Guillot, 2003; Hattori and Guillot, 2007). Hydrous fluids produced by prograde dehydration reactions within a slab generally bear a low elemental cargo (Schneider and Eggler, 1986; Manning, 2004; Spandler et al., 2007) and have minor effect onto compositional varieties of the mantle due to their relatively limited transfer along and above slabs (Philippot and Selverstone, 1991). However, they may significantly affect the mantle melting by lowering the peridotite solidus and modify the redox state through both fluid-buffered reaction and redox melting (e.g., Song et al., 2009). Previous studies of forearc peridotites revealed an oxygen fugacity range vary from those of mid-ocean ridge (MOR) mantle (down to FMQ-2) to much more oxidized resembled by arc xenolith peridotites (normally above FMQ) (Parkinson and Pearce, 1998; Parkinson and Arculus, 1999; Pearce et al., 2000; Dare et al., 2009; Birner et al., 2017). More oxidized conditions recorded in some supra-subduction peridotites are thus interpreted to result from peridotite infiltration by slab-derived hydrous fluids and melts (Parkinson and Arculus, 1999; Foley, 2011), although the exact mechanisms of mantle oxidation (e.g., by preferential Fe^{3+} transfer from the slab or direct oxidation by sulfate-rich slab fluids) yet may be not straightforward.

Here, we present the results of detailed petrographic, mineralogical and geochemical studies of mantle peridotites from the Khara-Nur massif (Eastern Sayan, southern Siberia), which represents the mantle section of the Mesoproterozoic SSZ ophiolites. The Khara-Nur peridotites resemble major- and trace-element composition of refractory forearc peridotites and testify to modification by supra-subduction melts. Along with that, the studied peridotites have evidently low $Fe^{3+}/\sum Fe$ ratios of Cr-spinel, which are unusual for typical supra-subduction zone

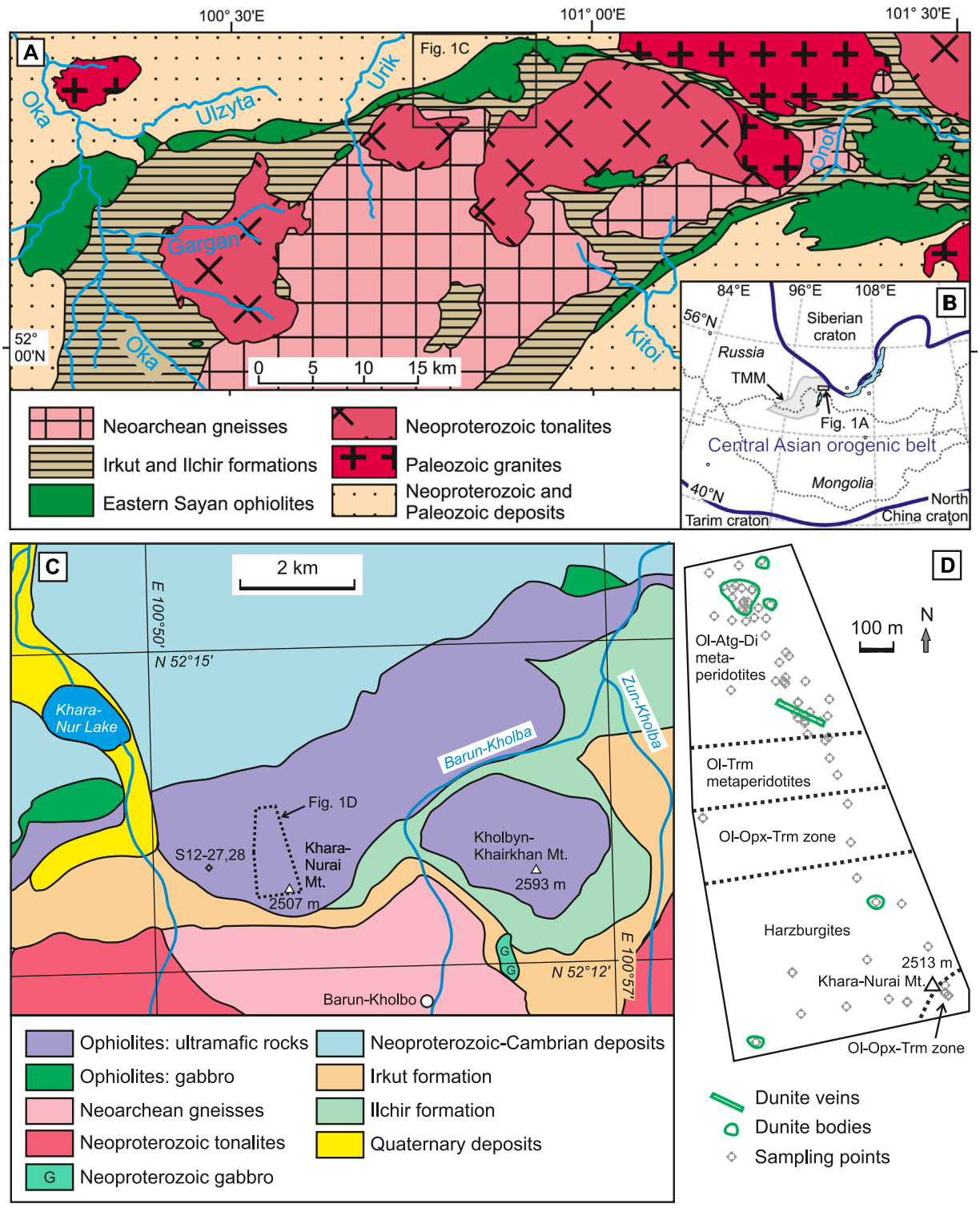

FIGURE 1
(A) Geological map of Gargan block and the Eastern Sayan ophiolites in the northern part of Tuva-Mongolian microcontinent (Kuzmichev, 2004; 2015) **(B)** General structure of the Central Asian orogenic belt and surrounding cratons (Kröner et al., 2017) with outlined Tuva-Mongolian microcontinent (TMM) **(C)** Detailed geological map of the Khara-Nur ultramafic massif and surrounding area, modified after (Suturin, 1978; Dobretsov et al., 1985; Skopintsev et al., 2021). The position of samples S12-27, 27/1, 28, 28/1 is marked **(D)** Geological scheme of detailed study area drawn by the authors of present work.

settings with the increased oxygen fugacities (fO_2). We compare the composition of Khara-Nur harzburgites with highly refractory harzburgites from oceanic islands and subcontinental lithospheric mantle in order to constrain the primary origin of these unusual peridotites.

2 Geological background

The Khara-Nur ultramafic massif is located in SE part of the Eastern Sayan range (southern Siberia), within the Tuva-Mongolian microcontinent of the Central Asian Orogenic belt (CAOB) (Figures 1A,B). The massif is part of the Eastern Sayan ophiolites overthrusting the Gargan continental block (Dobretsov et al., 1985). The Gargan block is composed of an Early Precambrian crystalline basement represented by tonalite gneisses, and covered by the Mesoproterozoic Irkut and Neoproterozoic Ilchir formations. The Irkut formation is represented by limestones and dolomites, and the Ilchir formation is composed of black shales and metabasalts. The Eastern Sayan ophiolite complex contains all members of ophiolite sequence, including mantle residual peridotites, mafic-ultramafic cumulates, sheeted dikes, and pillow lavas (Dobretsov et al., 1985). The lavas and sheeted dikes are represented by boninites and island-arc tholeiites, and mafic-ultramafic cumulate rocks assumingly crystallized from these melts (Sklyarov et al., 2016; Belyaev et al., 2017). The presence of boninites and IAT in the Eastern Sayan ophiolite points at their supra-subduction zone (SSZ) origin according to classification of Dilek and Furnes (2011) and, more specifically, indicates their affinity to forearc ophiolites, which are relatively abundant in CAOB (Furnes and Safonova, 2018; Yang et al., 2022). The regional greenschist metamorphism overprinted the Irkut and Ilchir formations (Dobretsov et al., 1985), whereas the early-stage seafloor metamorphism affected a crustal part of the ophiolite (Sklyarov and Dobretsov, 1987). The Eastern Sayan ophiolites were formed in the Late Mesoproterozoic (1,020 Ma; U-Pb on zircon from plagiogranites (Khain et al., 2002)). The ophiolites are covered by terrigenous rocks of the Dunzhugur formation with the oldest detrital zircon cluster of ~1,034 Ma, which is assigned to the onset of the Dunzhugur oceanic arc (Kuzmichev and Larionov, 2013). The remnants of this arc probably include Latest Mesoproterozoic metamorphosed volcaniclastic rocks of the Butugol block with a mean U-Pb zircon age of 1,009 ± 8 Ma (Shkolnik et al., 2023), located SW of the Gargan block within the Tuva-Mongolian microcontinent. The Ospin peridotite massif of the Eastern Sayan ophiolites is intruded by tonalites with U-Pb zircon age of 853 ± 10 Ma and Ar-Ar amphibole age of 855.8 ± 5.1 Ma (Damdinov et al., 2020). The age of Eastern Sayan ophiolite emplacement is also constrained by whole-rock Ar-Ar age of 799 ± 11 Ma, obtained for mafic dike cutting the Ulan-Sardag peridotite massif (Kiseleva et al., 2022). The tonalite intrusions of the Sumsunur complex formed at 785 ± 11 Ma within the Gargan block (Kuzmichev, 2004). Based on these data, Kuzmichev (2004), Kuzmichev (2015) considered the Meso- to Neoproterozoic evolution of the study area from the ophiolite formation in a forearc part of the Dunzhugur island arc to subsequent ophiolite obduction onto the passive margin of the Gargan block as a result of arc-continent collision, and a shift to an active continental-margin setting as exemplified by tonalite intrusions of the Sumsunur complex.

The Khara-Nur massif of ultramafic rocks traces the border between the Gargan block and Neoproterozoic-Cambrian sedimentary and volcanogenic strata, has an elongated shape of 25 km length and 1–7 km width (Figure 1C) and tectonic contacts with associated gabbro and pyroxenites representing the crustal part of the ophiolite. The Khara-Nur massif is composed of serpentinized dunites and harzburgites, serpentinites and talk-carbonate rocks (Pinus and Kolesnik, 1966; Suturin, 1978). Serpentinites and talc-carbonate rocks are exposed at western part and along the southern and northern borders of the Khara-Nur massif. According to our observations, a major part of the massif is composed of olivine-antigorite-diopside rocks, antigorite serpentinites and talc-carbonate rocks. The harzburgites are exposed at Khara-Nur (Ulan-Khoda) mountain, the top part of the massif. Detailed and continuous sampling located to the north of Khara-Nur mountain allowed distinguishing the relationships between distinct types of ultramafic rock; in northern direction, harzburgites are replaced by olivine-tremolite (Ol-Tr) metaperidotites and further by olivine-antigorite-diopside (Ol-Atg-Di) metaperidotites (Figure 1D). A narrow zone of Ol-Opx-Trm rocks is revealed in between, where harzburgites exhibit the development of tremolite and secondary olivine rims around orthopyroxene, whereas no talc- or anthophyllite-bearing varieties were identified. The lenses and veins of dunites are found among harzburgites and Ol-Atg-Di metaperidotites.

3 Analytical methods

Major oxides in whole-rock samples were analyzed by X-ray fluorescence (XRF) analysis using Bruker S8 Tiger spectrometer. To perform the analysis, rock powders (~110 mg weight) were fused with a mixture of lithium metaborate and lithium tetraborate with the addition of LiBr solution. The methodology is described by Amosova et al. (2015).

The major element composition of the minerals was acquired by electron probe micro analysis (EPMA) using a JEOL JXA-8200 electron-probe microanalyzer equipped with five wavelength dispersive spectrometers (WDX), and Tescan MIRA 3 LMH scanning electron microscope (SEM) equipped with Oxford instruments Ultim MAX 40 energy-dispersive spectrometer (EDX). These measurements were performed at the Center of Isotope-Geochemical Studies of IGC SB RAS (Skuzovatov et al., 2022). The EPMA-WDX instrument operated at an accelerating voltage of 20 kV, beam current of 20 nA, and beam size of 1 μm. The counting time was 10 s for peak acquisition, and 5 s for background. Albite, olivine, diopside, pyrope, orthoclase, ilmenite, chromite, Mn-garnet, apatite and phlogopite were used as calibration standards. SEM-EDX measurements were carried out at an accelerating voltage of 20 kV and counting times of 10–15 s. The back-scattered electron images (BSE) along with observations using the Olympus BX-51 petrographic microscope were used to reveal the textural features of the studied rocks.

The composition of Cr-spinel was also studied at the Analytical Center for Multi-Elemental and Isotope Research, Siberian Branch,

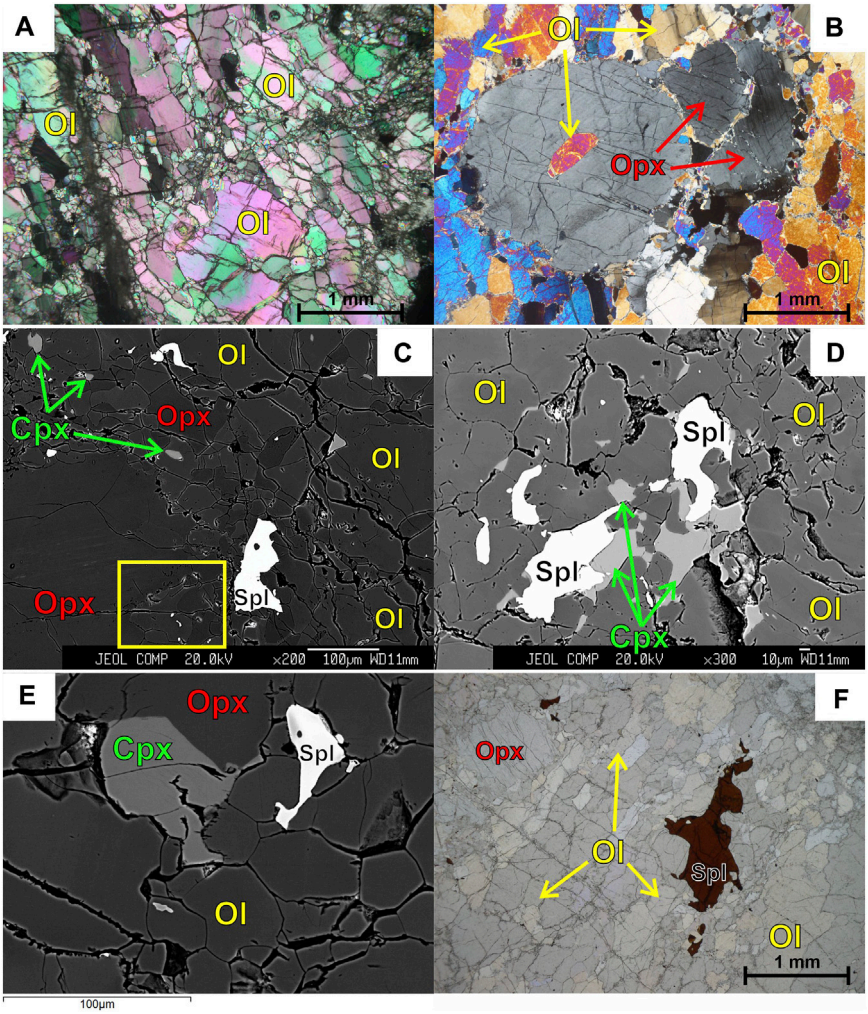

FIGURE 2
Photomicrographs of representative microstructures of the Khara-Nur harzburgites **(A)** Elongated olivine porphyroclasts with linear orientation and small grains of olivine, sample S12-28 **(B)** Orthopyroxene porphyroclasts with olivine inclusion and kink-bands, sample S21-88; **(C)** Newly-formed grains of clinopyroxene, olivine, and spinel near to orthopyroxene porphyroclast; newly-formed olivine contains inclusions of Cr-spinel and clinopyroxene, sample S12-28 **(D)** Intergrowth of newly-formed clinopyroxene and Cr-spinel, sample S21-92; **(E)** Replacement of orthopyroxene by newly-formed clinopyroxene, sample S12-27 **(F)** Residual Cr-spinel with irregular shape, S21-88. Crossed-polarized light in **(A and B)**, plane-polarized light in **(F)**, backscattered electron (BSE) images in **(C, D, E)**. Hereafter, Ol—olivine, Opx—orthopyroxene, Cpx—clinopyroxene, Spl—Cr-spinel.

Russian Academy of Sciences (Novosibirsk), using a MIRA 3 LMU scanning electron microscope (Tescan Orsay Holding) equipped with an AZtec Energy XMax-50 X-ray microanalysis system (Oxford Instruments Nanoanalysis Ltd.) at an accelerating voltage of 20 keV and an electron beam current of 1.4 nA. The live time of spectrum acquisition was 60 s, while the total number of registered X-ray quanta in the spectra reached (1.4—1.5) x 10^6. The standards used were simple compounds of Al_2O_3 for Al and O, SiO_2 for Si, pure metals Ti, V, Cr, Mn, Fe, Ni, Zn, as well as diopside ($CaMgSi_2O_6$) for Mg and calcium pyrophosphate ($Ca_2P_2O_7$) for Ca. The intensity of the K-series radiation of the analyzed elements was used as an analytical signal, the matrix corrections were taken into account by the XPP method implemented in the software of the Aztec Energy microanalysis system. Under these analysis conditions, the detection limit (3σ) of impurities is (weight %): SiO_2—0.13, CaO—0.08, TiO_2—0.10, V_2O_3—0.09, MnO—0.23, NiO—0.15, ZnO—0.19. The random error of analysis for the main components at 12% MgO, 20% Al_2O_3, 50% Cr_2O_3, and 17% FeO does not exceed 0.7, 0.5, 0.3, and 0.6 rel. %, respectively. To compensate for the drift of the probe current, all the results of the analysis were normalized to the intensity of the *K*-series Co lines of the spectra of metallic cobalt acquired every 2–3 h of the analytical session. The $Fe^{3+}/\sum Fe$ ratio was calculated assuming the ideal stoichiometry of the spinel composition, i.e., the ratio of cations to anions is 3:4. However, the correctness of such calculations is not always justified due to the presence of systematic errors in determining the concentrations of the main components of spinel, primarily due to the imperfection of the system of matrix corrections. To improve the accuracy of the assessment of the degree of iron oxidation by the EPMA method, we used as secondary standards 6 samples of spinels (Vi314-320, 8,601-10, 4,334-14, 8,505-2, 8,803-3, 8,601-3), kindly provided by D.A. Ionov. The composition of these samples varies significantly in the content of Al_2O_3 (22%–64%), Cr_2O_3 (4%–47%), FeO (11%–17%) and MgO (15%–21%). The $Fe^{3+}/\sum Fe$ ratio of the secondary

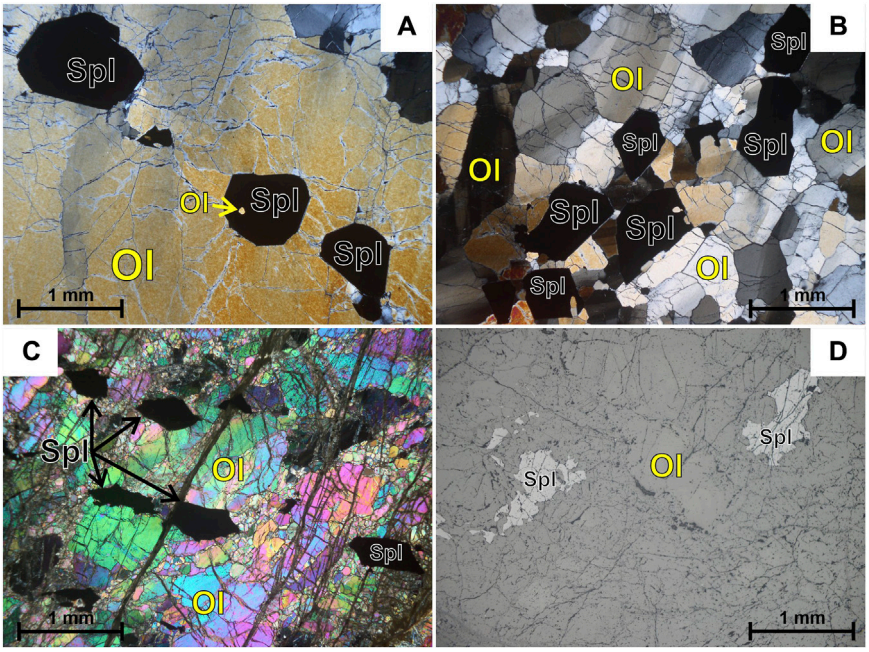

FIGURE 3
Photomicrographs of representative microstructures of the Khara-Nur dunites **(A)** Large olivine porphyroclast with kink-bands, containing euhedral Cr-spinel grains, sample S18-116 **(B)** The chain of euhedral Cr-spinel grains among small grains of olivine demonstrating kink-bands, sample S18-116; **(C)** Dunite with porphyroclastic texture, containing chain of anhedral to subhedral Cr-spinel grains, sample S18-133 **(D)** Residual irregular Cr-spinel grains among olivine, sample S21-89.

standards according to Mössbauer spectroscopy data varies within 0.125—0.22 (Ionov and Wood, 1992). Based on the results of the analysis of these samples according to the method described above, we have established the dependence of the deviation of the calculated value of the ratio $Fe^{3+}/\sum Fe$ according to EPMA data from the Mössbauer spectroscopy data:

$$Delta = a + bCr_m + cAl_m$$

where a, b, c are empirical factors, Cr_m and Al_m are mass fractions of chromium and aluminum. The graph (Supplementary Figure 1) of the dependence of the observed deviations of iron oxidation from that predicted by the regression model for a set of secondary standards indicates the possibility of successful usage of this model to correct the results of calculating the proportion of oxidized iron according to the results of EPMA. The limitation of using this model may be either a significant difference in the chemical composition of the samples from the composition of the secondary standards, for example, a high content of chromium or iron oxides, or a significant deviation of the iron oxidation from the range of iron oxidation in the secondary standards.

In-situ trace element composition of silicate minerals (olivine, orthopyroxene, clinopyroxene, amphibole) was determined using laser-ablation inductively coupled plasma mass spectrometry (LA-ICP-MS) at the Center for Geodynamics and Geochronology at the Institute of the Earth's Crust SB RAS (Irkutsk, Russia) and secondary-ion mass-spectrometry (SIMS) at the Yaroslavl Branch of the Institute of Physics and Technology RAS (PTIAS, Yaroslavl, Russia). Selected grains of olivine and orthopyroxene with enough space (>100 μm in size) were analyzed by LA-ICP-MS and utilized an Agilent 7,900 quadrupole mass-spectrometer coupled with the Analyte Excite 193 nm excimer ArF laser with HelEx II cell. NIST 612 and 614 standard reference materials (SRM) were used for the initial calibration by bracketing, and BCR-2G and BIR-1G basalt glass standards were used to control the accuracy and reproducibility of analyses. All samples and standards were analyzed under the same measurement conditions, which included background measurement for 30 s, sample analysis for 90 s, laser beam diameter of 110 μm, energy of 3.5 J/cm^2, and pulse frequency 10 Hz. The flow values of the cooling gas, plasma-forming gas, and additive Ar were 16.0, 1.0, and 1.0 L/min, respectively. Helium with a purity of 6.0 and a flow rate of 1.0 L/min was used as a carrier gas. The energy of the plasma was 1550 W. The trace element content in the largest (up to 2–4 mm) grains of olivine and orthopyroxene was measured in a raster scanning mode with laser beam (110 μm in diameter) continuously moved within the 800x600 μm rectangular field. All calculations and data reduction used Iolite 4 software. ^{29}Si contents of silicates based on SiO_2 contents as determined by EPMA and SEM-EDX methods were used as internal standards.

Trace element contents in small grains of silicate minerals (<100 μm) and spinel-hosted multiphase silicate inclusion phases were determined by SIMS using a Cameca IMS-4f mass-spectrometer. Spot analyses were done at a focused primary beam of O^{2-} ions with an energy of 14.5 keV, a spot size of 20 μm, and a current intensity of primary ion beam of 8 nA. Each measurement included 5 cycles with about 50 min total acquisition time for one point. Element concentrations were

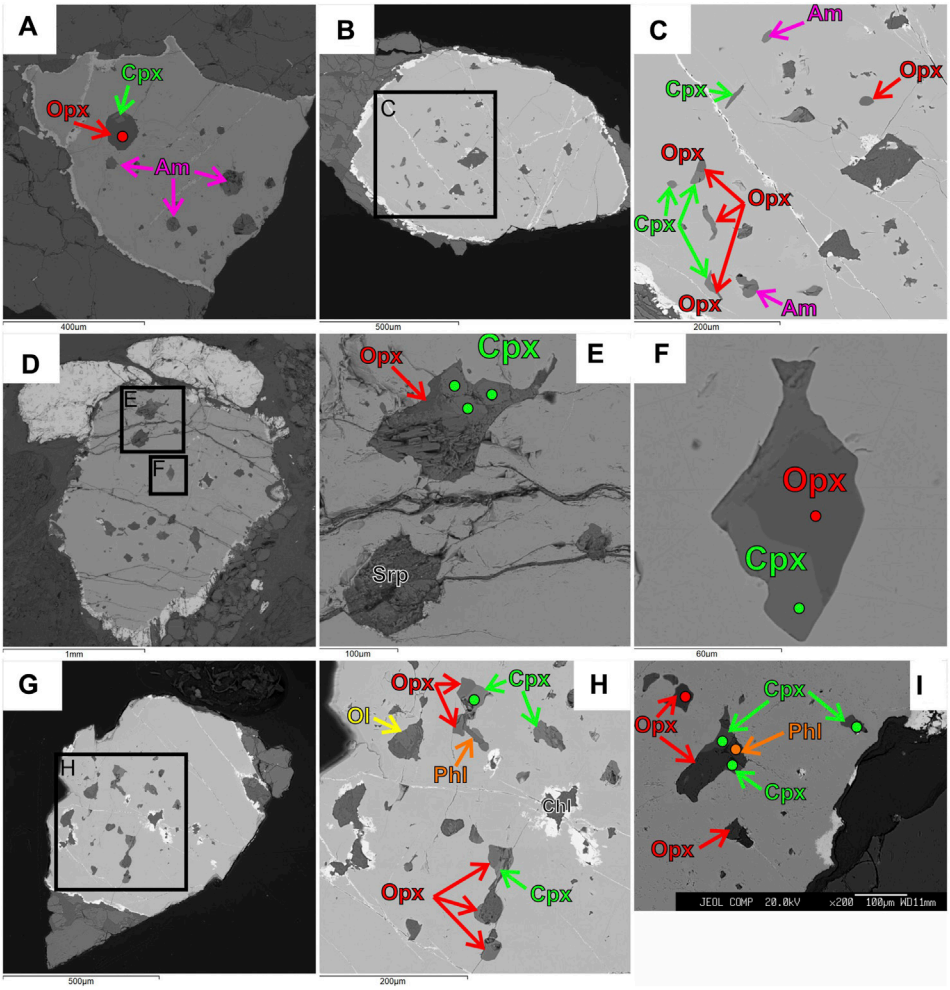

FIGURE 4
Photomicrographs (BSE images) of representative Cr-spinel grains containing multiphase mineral inclusions in the Khara-Nur dunites. Distribution of typical single- and poly-phase inclusions in Cr-spinel grains of sample S18-12 **(A-C, G, H)** and sample S18-12/6 **(D, E, F, I)**. BSE images. Colored dots mark the location of the SIMS analysis. Am—amphibole, Phl—phlogopite, Srp—serpentine, Chl—chlorite.

determined using ^{30}Si (measured by EPMA and EDX) as an internal standard. Corrections for Gd, Yb, Eu, and Er were calculated according to the method (Bottazzi et al., 1994).

4 Results

4.1 Petrography and microstructures of peridotites

The modal amounts of olivine (Ol) in the studied harzburgites vary within 73%–86%, that of orthopyroxene (Opx)—26%–12.5%, clinopyroxene (Cpx)—0.6%–2%, Cr-spinel (Cr-Sp)—0.4%–0.5%. The rocks exhibit porphyroclastic textures, with Ol and Opx porphyroclasts up to 1–3 mm in size, and small grains of Ol and Opx 0.1–0.3 mm in size (Figures 2A,B). A linear orientation of elongated Ol porphyroclasts is observed (Figure 2A). The porphyroclasts of Ol and Opx exhibit kink-bands and undulose extinction (Figure 2B). The observations using SEM/EDX revealed narrow (less than 1 µm wide) oriented ingrowths of Cr-Sp, which are interpreted as exsolution lamellae. The porphyroclasts of Opx often have rounded shapes and rarer concave margins, form grain clusters. The Opx porphyroclasts also contain clinopyroxene exsolution lamellae, which lack in small Opx grains; in some cases bear Ol inclusions in their central parts (Figure 2B). More often, small Ol grains are developed around Opx porphyroclasts and along cracks, which cross the porphyroclasts. Newly-formed, small grains of Cpx, Cr-Sp, rarely edenite, and Ol are observed close to the Opx porphyroclasts and among the small grains of olivine and orthopyroxene (Figures 2D,E). The newly-formed small Ol grains bear small inclusions of Cr-Sp.

Clinopyroxene composes irregular grains (10–100 µm in size) without exsolution lamellae, which are located near to small Opx and locally indicate replacement of Opx by Cpx (Figure 2E). In addition, Cpx forms intergrowths with small irregular Cr-Sp. Homogeneous porphyroclasts of Cr-Sp generally have irregular shape and size up to 1.5 mm, and are located in the interstitial

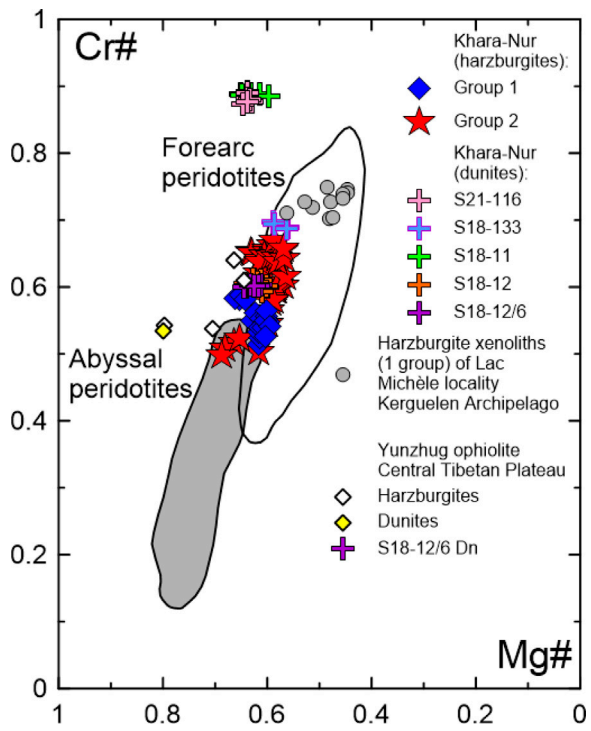

FIGURE 5
Cr/(Cr + Al) vs Mg/(Mg + Fe2+) in Cr-spinels of Khara-Nur peridotites of both groups (Group 1—blue and Group 2—red symbols). Harzburgites and dunites of Yunzhug ophiolite (Huang et al., 2020), harzburgite xenoliths of Lac Michèle locality of Kerguelen Archipelago (Wasilewski et al., 2017), fields of abyssal (Dick and Bullen, 1984) and forearc peridotites (Ishii et al., 1992; Parkinson and Pearce, 1998) are shown for comparison.

space (Figure 2F). Accessory sulfides are represented by pentlandite and found as inclusions in silicates and in the interstitial space. The secondary minerals are represented by antigorite, lizardite, talc, fibrous chlorite, formed due to low-temperature serpentinization. The amount of secondary minerals in harzburgites does not exceed 1%.

Most of dunites are composed of Ol (>90 vol%) and Cr-Sp (1-3 vol%) and lack pyroxenes, except the S21-89 sample, which has 8.5 vol% of Opx and 0.5 vol% of Cpx. Dunites have porphyroclastic textures (Figures 3A–C), with Ol porphyroclasts up to 1–5 mm and small grains of Ol 0.1–0.5 mm in size. Kink-bands in olivine are also observed. Ol porphyroclasts contain narrow oriented plates of Cr-spinel. In the S21-89 sample, Cr-Sp has irregular shape, whereas in other dunites, Cr-spinel is anhedral to subhedral. Cr-Sp grains form chains, which are located both in porphyroclasts and small grains of olivine in some samples (S18-11, S18–12, S18-12/6). The veinlets of antigorite are present in dunites as well.

Cr-Sp in duinte bear silicate inclusions, which are interpreted as trapped and crystallized batches of the former silicate melt. Such melt inclusions were found in three dunites; one sample (S18-11) only has small inclusions cut by cracks and completely replaced by chlorite, whereas in the S18–12 and S18-12/6 dunites, the inclusions are irregular-shaped and orbicular (Figure 4). The inclusions are arranged irregularly within the host Cr-Sp, and their size ranges from 20 to 40 μm (generally single-phase) to 150–200 μm (polyphase inclusions). The multiphase inclusions are composed of Ol, pyroxenes (diopside and enstatite), Amp (Mg-pargasite, Mg-hastingsite, edenite, tschermakite), and phlogopite (Figure 4; Supplementary Table S2). A single melt inclusion contain up to 3 exposed phases (e.g., Cpx+Opx+Phl or Cpx+Ol+Phl), while some of the inclusions are composed of two phases (most often Cpx+Opx, Cpx+Amp, or Opx+Amp), or a single phase (Ol, Cpx, Opx, or Amp). Some of the inclusions are cracked and underwent secondary alteration, expressed as development of serpentine and chlorite (Figures 4E,H). Secondary magnetite develops on the contact between serpentinized inclusions and host Cr-Sp (Figures 4C,H) and forms rims around the Cr-Sp.

4.2 Whole-rock major-element composition

The Khara-Nur harzburgites have very low losses on ignition (LOI) within 0–0.41 wt% (Supplementary Table S1). Relative to depleted mantle (DM) composition, the rocks are richer in MgO (45.9–48.4 wt%) and strongly depleted in Al_2O_3 (0.39–1.05 wt%), CaO (0.27–0.49 wt%), Na_2O (b.d.l.), and K_2O (b.d.l.). In dunites, the LOI values are slightly higher (0.84-1.89 wt%). As compared to harzburgites, the dunites exhibit lower SiO_2 (40–42 wt%), CaO (<0.1–0.4 wt%), Al_2O_3 (<0.1–0.5 wt%), but higher MgO (48.3–51.7 wt%) and Cr_2O_3 (0.43-1.94 wt%). NiO abundances in the samples of two types are similar (0.3–0.33 wt% in harburgites versus 0.29–0.36 wt% in dunites).

4.3 Mineral major-element composition

Cr-Spinel from harzburgites has high values of Cr# (Cr/(Cr + Al)) within 0.51–0.66 and Mg# (Mg/(Mg + Fe^{2+})) within 0.58–0.66 (Supplementary Table S2; Figure 5). In some dunite samples (S18–12, S18-133), Cr-Sp has the composition similar to that from harzburgites, while higher Cr# (0.87–0.89) and lower Mg# (0.52–0.65) are typical for the rest dunites (samples S18–11, S21-116). The TiO_2 contents in Cr-Sp from harzburgites is below 0.1 wt %, while slightly higher values (from <0.1 wt% to 0.15 wt%) were revealed occasionally in dunites. In harzburgites, there is a systematic decrease in Cr# and an increase in Mg# towards the rims of Cr-Sp porphyroclasts; newly formed, small Cr-Sp grains resemble the composition of porphyroclast rims or exhibit even lower Cr# and higher Mg#. Cr-Sp from both harzburgites and dunites are characterized by low $Fe^{3+}/\sum Fe$ ratios of 0.02–0.12 obtained with correction methods using a set of secondary standards with $Fe^{3+}/\sum Fe$ ratios measured by Mössbauer spectroscopy (Supplementary Table S2). In small Cr-Sp grains from harzburgites, $Fe^{3+}/\sum Fe$ ratios are slightly higher (up to 5-30 rel. %) (Supplementary Table S2).

Olivine porphyroclasts in harzburgites are homogeneous, display high Mg# within 0.912–0.927 and NiO within 0.37–0.47 wt% (Supplementary Table S2; Figure 6). Ol porphyroclasts from some dunites (samples S18–12, S18-133) have Mg# of 0.916–0.925, similar to that of Ol from harzburgites. In the other dunite samples (S18–11, S21-116), Ol porphyroclasts

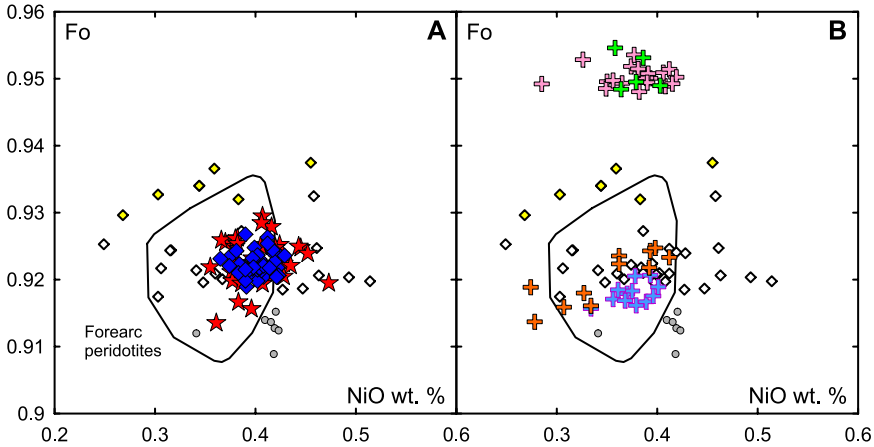

FIGURE 6
NiO content vs Fo of olivine in Khara-Nur harzburgites **(A)** and dunites **(B)**. All symbols are as in Figure 5. Field of forearc peridotites is from (Ishii et al., 1992; Parkinson and Pearce, 1998).

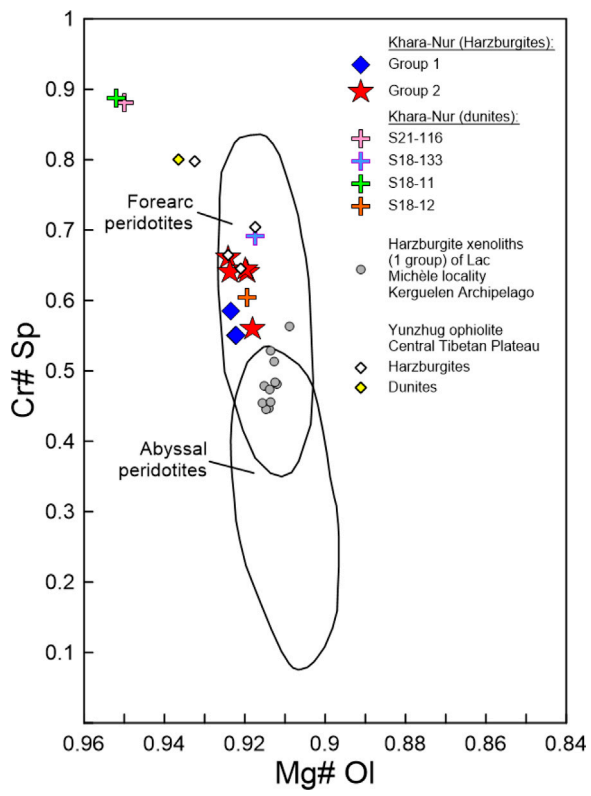

FIGURE 7
Cr/(Cr + Al) of Cr-spinel vs Fo of olivine. All symbols and fields are as in Figure 5.

have higher Mg# near 0.95. In addition, Ol porphyroclasts in dunites and harzburgites are characterized by similar NiO contents. In harzburgites, the relation of Cr# in Cr-Sp and Mg# in Ol is similar to that of forearc peridotites (Figure 7).

Orthopyroxene from harzburgites (Supplementary Table S2; Figures 8A,B) is high-Mg# (0.918–0.935) and characterized by low contents of Al_2O_3 (0.5–2.6 wt%), Cr_2O_3 (0.4–1.0 wt%) and very low TiO_2 and Na_2O (b.d.l.). The rims of Opx porphyroclasts have lower Al_2O_3 and Cr_2O_3 contents at similar Mg# relative to the cores. The small grains of Opx have the composition of porphyroclasts or even lower Al_2O_3 and Cr_2O_3. Cpx from harzburgites (Supplementary Table S2; Figures 8C,D) are high-Mg# (0.942–0.957), and have low contents of Al_2O_3 (0.6–2.5 wt %), Cr_2O_3 (0.4–2.0 wt%) and Na_2O (b.d.l.—0.3 wt%).

Orthopyroxene and Cpx from melt inclusions in Cr-Sp from dunites (Supplementary Table S2; Figure 8) have high Mg# (0.925–0.935 and 0.94–0.95, respectively), varying contents of Al_2O_3 (0.6–1.48 wt% and 0.81–3.06 wt%, respectively) and Cr_2O_3 (0.57–1.20 wt% and 0.8-2.0 wt%, respectively). In terms of Mg#, pyroxenes in inclusions closely resemble the composition of matrix pyroxenes from the Khara-Nur harzburgites and differ from that of the Eastern Sayan ophiolite cumulates (Figure 8).

Amphibole from harzburgites is represented by pargasite and edenite. Amphibole from inclusions in Cr-spinel of dunites is represented mainly by pargasite and edenite, and rarely by magnesian hornblende (Supplementary Table S2). Pargasite and edenite have high Mg# (0.936–0.944 and 0.939–0.953, respectively) and low TiO_2 content (~0.4–0.52 and 0.37–0.52). Phl in Cr-Sp-hosted inclusions is rare and possesses high Mg# (0.97–0.98) and low TiO_2 content (~0.55 wt%).

4.4 Mineral trace-element composition

Orthopyroxene from harzburgites (Supplementary Table S2) has low contents of trace elements (Figures 9A,B), which are, in some samples, below the detection limits for some elements. The chondrite-normalized rare-element element (REE) patterns have positive slopes of HREE and flat or slightly negative slopes of LREE, with $LREE_N$<$HREE_N$ (Figure 9A), which indicate more depleted REE composition of the Khara-Nur Opx relative to that

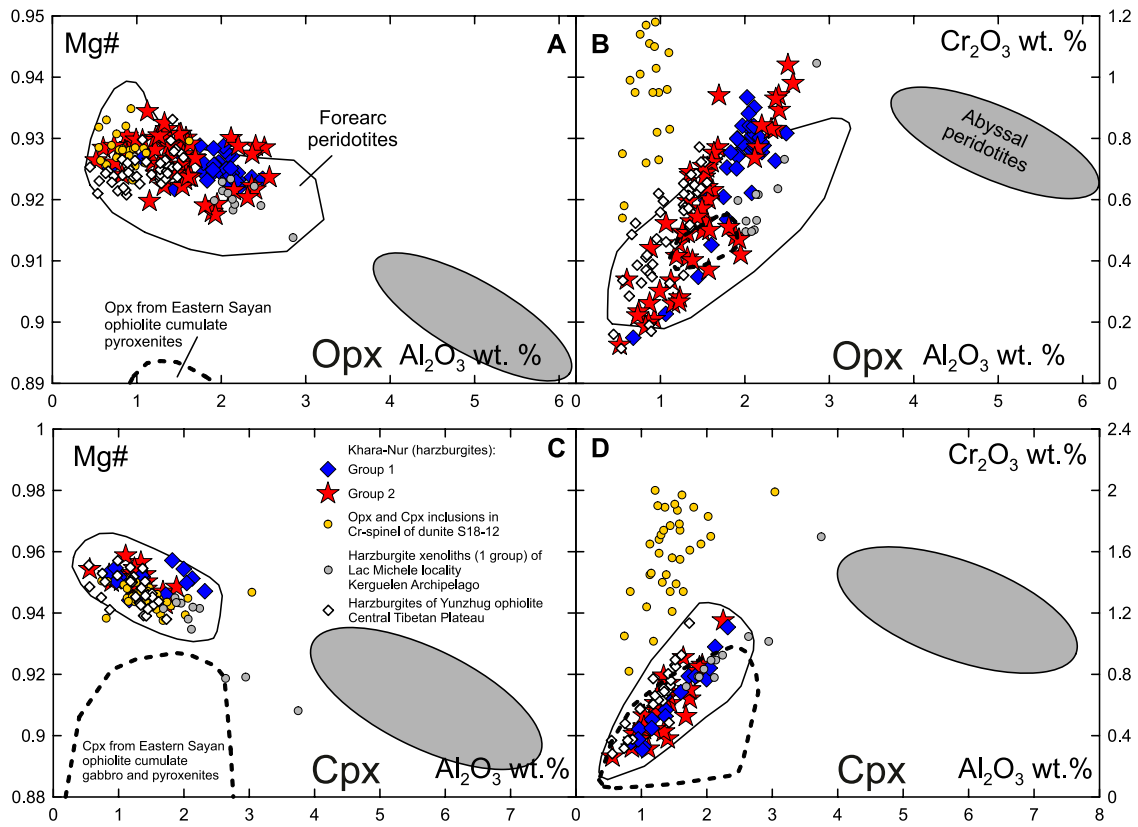

FIGURE 8
Major-element compositions of orthopyroxene **(A, B)** and clinopyroxene **(C, D)** from the Khara-Nur harzburgites and inclusions in Cr-spinel of Khara-Nur dunites. Fields of abyssal peridotites (Hellebrand, 2002; Seyler et al., 2003), forearc peridotites (Ishii et al., 1992), pyroxenes of cumulates from Eastern Sayan ophiolites (unpublished data of the authors) are shown for comparison. Other symbols are as in Figure 5.

from abyssal peridotites (Figure 9A). Trace-element patterns are U-shaped with Cs and Ba enrichment, prominent positive Pb anomaly, and weak negative Nb and Zr anomalies (Figure 9B). The observed positive anomalies of Ti support highly depleted nature of the rocks (McDade et al., 2003). More specifically, trace element patterns are similar to that of Opx from supra-subduction peridotites (Figure 9B), for instance, from peridotite xenoliths of the Bismark arc (Tollan et al., 2017) and forearc peridotites of Egypt (Khedr et al., 2022). Opx from Cr-Sp-hosted inclusions have similar HREE contents and higher L-MREE contents relative to Opx from harzburgites (Figure 9C), while their trace element patterns demonstrate positive anomalies of Pb (Figure 9D).

Clinopyroxene from harzburgites is characterized by low contents of trace elements (Supplementary Table S2). In most samples, Cpx has similar REE patterns with a decrease from HREE to MREE and LREE variations, generally with $LREE_N$<$HREE_N$. Almost flat REE distribution patterns are observed in Cpx from three harzburgite samples. All Cpx demonstrate enrichment in Cs and positive anomalies of Nb and Pb (Figure 10B). HREE contents in Cpx of the Khara-Nur harzburgites are lower than in Cpx from abyssal peridotites and approach that of peridotites from forearcs and supra-subduction settings (Figure 10A).

Clinopyroxene from inclusions in Cr-Sp exhibit two types of trace element distribution. Except one analysis, it displays flat distribution of HREE, enrichment in MREE and LREE over HREE, and generally demonstrates a positive slope from La to Nd (type 1; Figure 10C). All but one Cpx exhibit weak negative anomalies of Eu. Most Cpx are enriched in Cs and Ba, show negative anomalies of Nb, Zr, Ti and Sr One inclusion-hosted Cpx demonstrates negative anomaly of Ba, and two others lack Sr anomaly. Moreover, Pb shows the most variable behavior with positive, negative, or lacking anomalies. Only one inclusion-hosted Cpx revealed almost flat distribution of REE (Figure 10C) at enrichment in Cs and Ba (type 2; Figure 10D). HREEs contents in Cpx of both types are similar and vary within 2–5 chondrite levels, while more significant variations (1–20) of LREE were found. Importantly, Cpx with both types of trace element patterns may be found in a single Cr-Sp (Figures 10C,D).

4.5 P–T estimates

The equilibrium temperatures were calculated using several geothermometers based on rock-forming and accessory phases (Supplementary Table S1). The highest temperature values were obtained by Opx-Cpx thermometer of Liang et al. (2013), based

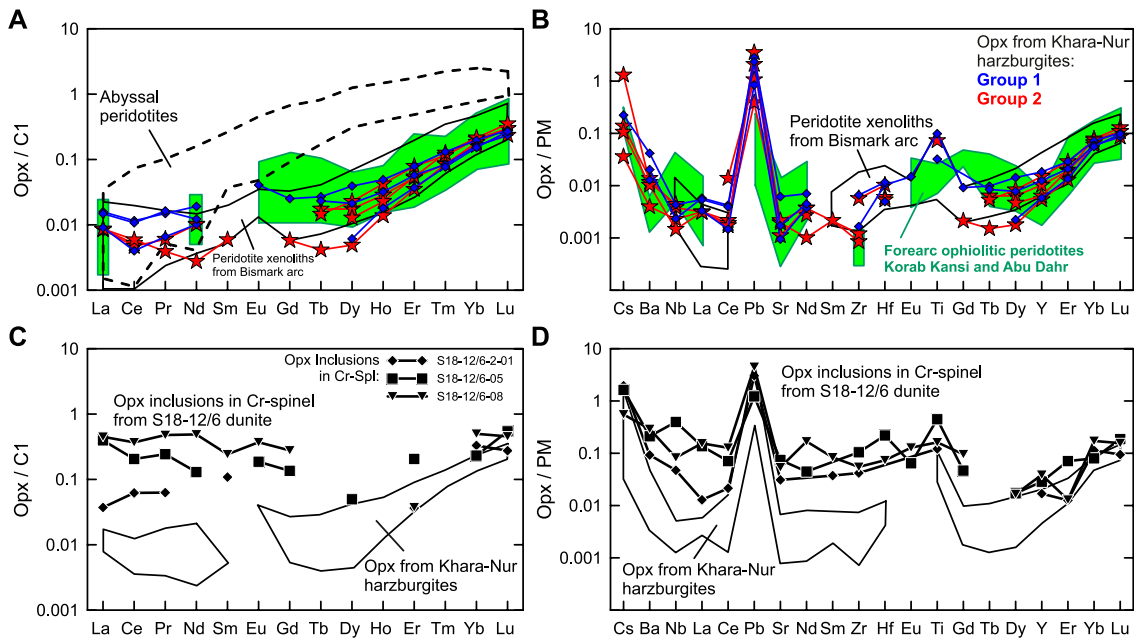

FIGURE 9
REE and trace element compositions of orthopyroxene from Khara-Nur harzburgites **(A, B)** and orthopyroxene from inclusions in Cr-spinel of Khara-Nur dunite **(C, D)**. Fields of orthopyroxene composition from abyssal peridotites (Hellebrand et al., 2005; Seyler et al., 2011), peridotite xenoliths from Bismark island arc (Tollan et al., 2017) and forearc-type ophiolite peridotite of Korab Kansi and Abu Dahr massifs, Egypt (Khedr et al., 2022) are shown for comparison. REE are normalized to C1-chondrite, trace elements to PM (Sun and McDonough, 1989).

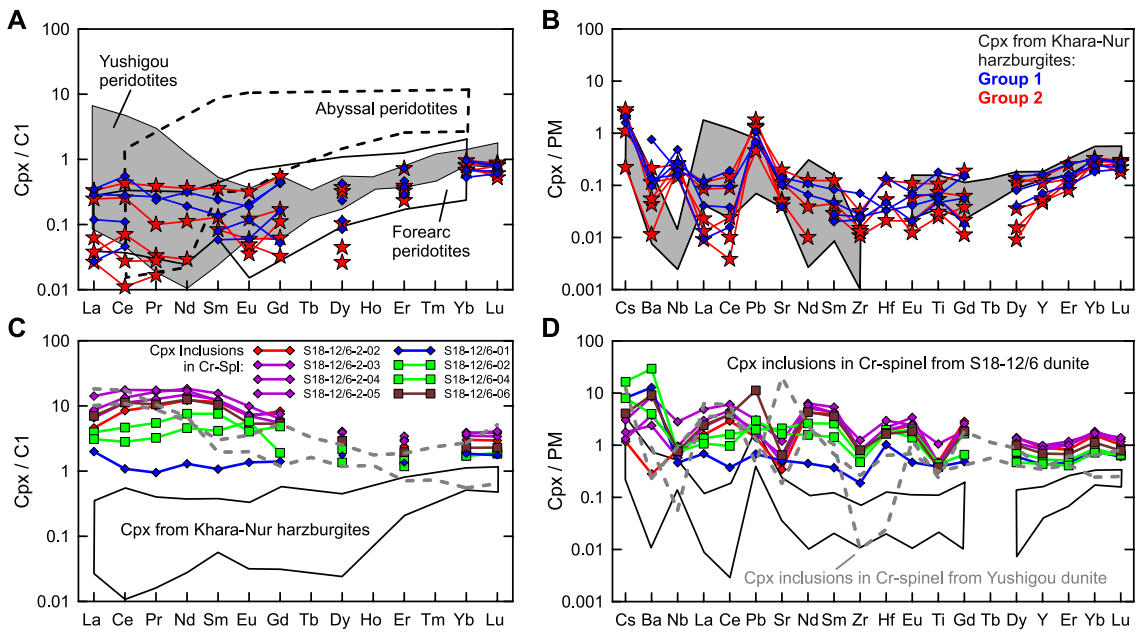

FIGURE 10
REE and trace element composition of clinopyroxene from Khara-Nur harzburgites **(A, B)** and clinopyroxene from inclusions in Cr-spinel of Khara-Nur dunite **(C, D)**. Fields of clinopyroxene from abyssal peridotites (Johnson et al., 1990), forearc peridotites (Parkinson et al., 1992; Bizimis et al., 2000) and peridotites of Yushigou ophiolite (Zhou et al., 2021) are shown for comparison. REE are normalized to C1-chondrite, trace elements to PM (Sun and McDonough, 1989).

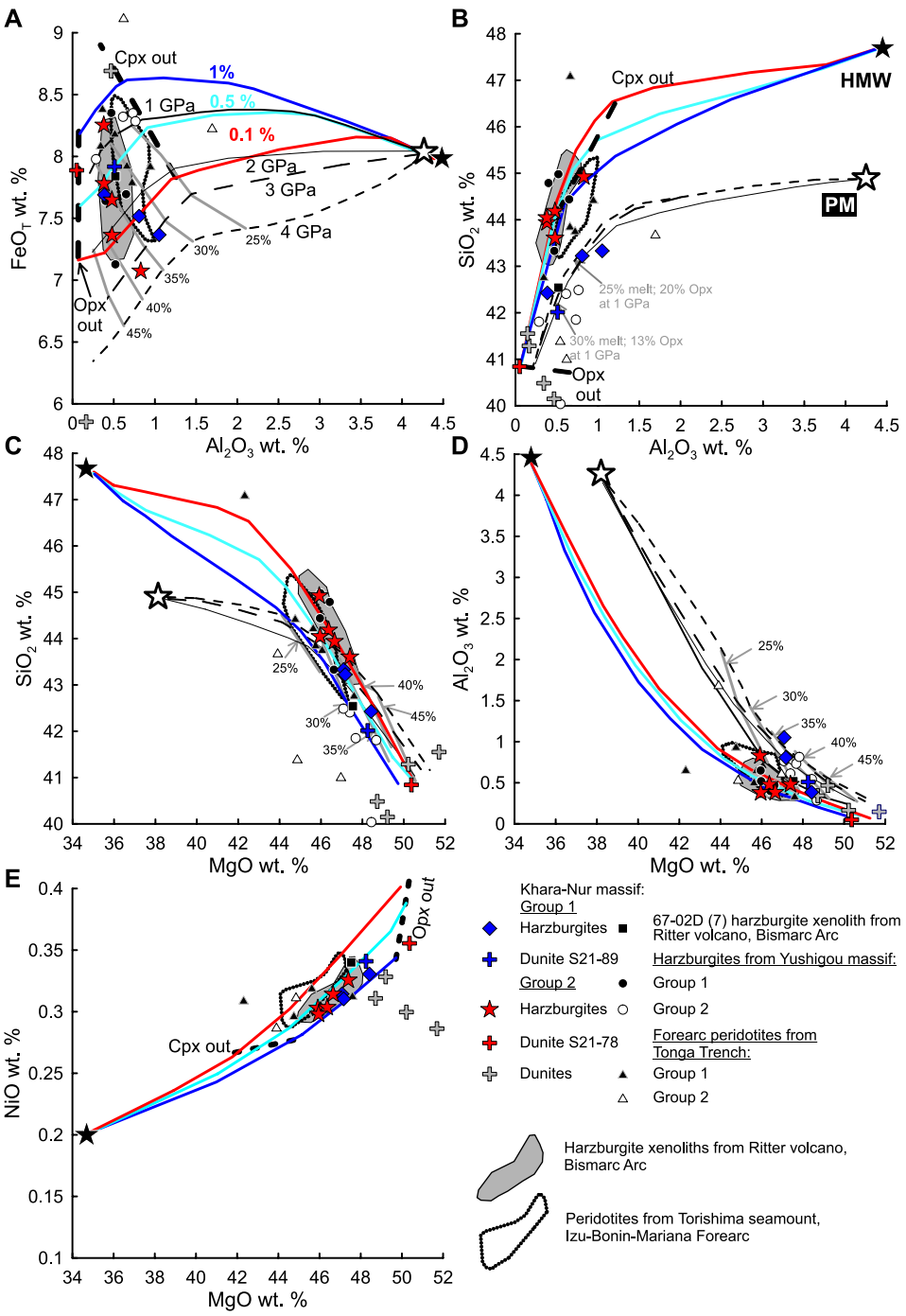

FIGURE 11
Co-variation plots of major element oxides for Khara-Nur peridotites **(A–E)**. Also shown are evolution trends for residues of anhydrous batch melting of fertile lherzolite at 1–4 GPa (black lines) and modelled hydrous batch melting of hybrid mantle wedge (HMW) peridotite at 1 GPa (colored lines) after (Bénard et al., 2017). Primitive mantle (PM) composition after (Palme and O'Neill, 2014), sample of harzburgite xenolith #67-02D (7) and grey field of other harzburgite xenoliths from Ritter volcano of Bismark arc (Bénard et al., 2017), harzburgites of Yushigou ophiolite massif, group 1 after (Song et al., 2009) and group 2 after (Zhou et al., 2021), forearc peridotites of Tonga trench (Birner et al., 2017), peridotites of Torishima seamount (Izu-Bonin-Mariana forearc) of (Parkinson and Pearce, 1998; Ionov, 2010) are shown for comparison.

on REE+Y distribution between two pyroxenes (862°C–1,093 °C). The most well reproduced temperature values were calculated from HREE and Y distribution, whereas LREEs distribution coefficients for pyroxene pairs deviate from the regression lines due to their slower diffusion rates. Similar temperatures were obtained by Ca-in-Opx and Al-in-Opx contents thermometers (1,000°C–1,114 °C and 935°C–1,056 °C, respectively) (Brey and Köhler, 1990; Köhler and Brey, 1990).

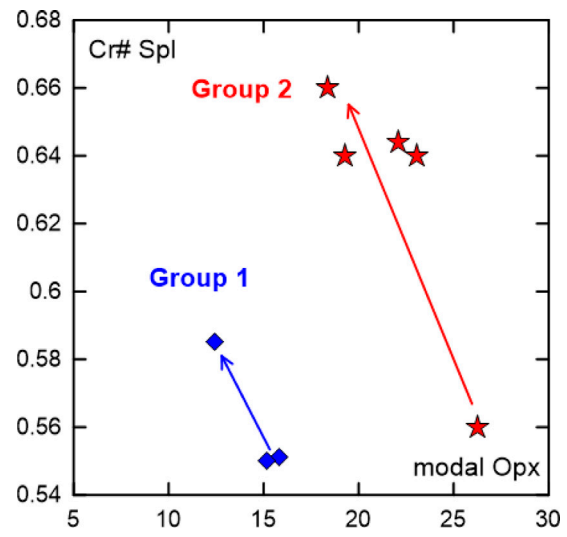

FIGURE 12
Plot of Cr# in Cr-spinel vs. modal orthopyroxene contents (in wt %) in Khara-Nur harzburgites of both groups. The arrows show the partial melting trends.

The lowest temperatures were obtained from thermometers using Fe^{2+}-Mg diffusion exchange. Two-pyroxene Fe-Mg thermometry (Brey and Köhler, 1990) yielded a range of 767°C–888 °C, whereas the values from Ol–Sp pairs (O'Neill and Wall, 1987; Ballhaus et al., 1991) are even lower (693°C–829 °C). In dunites, the temperature values from Ol-Sp thermometry are within 770°C–859 °C, which is similar to those estimated for harzburgites by the same thermometer. In Cr-spinel-hosted inclusions in S18-12 dunite, the clinopyroxene crystallization temperature estimated from the geothermometer (Wang et al., 2021) is 1,258 °C, and the amphibole crystallization temperature calculated from the geothermometer (Ridolfi et al., 2010) is 940 °C (Supplementary Table S1). The equilibrium temperatures calculated from two-pyroxene Fe-Mg (767°C–888 °C) and REE+Y geothermometry (891°C–1,089 °C) for Khara-Nur harzburgites are within the range for supra-subduction peridotites and lower than estimates for the abyssal peridotites (Dygert and Liang, 2015; Tollan et al., 2017).

5 Discussion

The textures, mineral and whole-rock compositions reflect highly depleted nature of the Khara-Nur harzburgites and resemble that of forearc peridotites (Figures 5–10). Low equilibrium temperatures (common for supra-subduction peridotites) support the location of Khara-Nur peridotites in the mantle wedge. Along with that, the microstructures of porphyroclastic harzburgites, the presence of newly formed minerals (Ol, Cpx, Cr-Sp) in the fine-grained matrix, LREE-MREE enrichment of Cpx, coupled with the presence of Sp-hosted multiphase inclusions of former melts crystallized at high temperatures in dunites provide evidence of melt-peridotite interaction in a mantle wedge setting. This is further supported by the reconstructed localization of the Khara-Nur peridotites in a Mesoproterozoic mantle wedge, their partial transformation into hydrous metaperidotites as a response to lower-temperature, high-pressure subduction metamorphism most likely close to subduction interface, and spatial association with boninitic and island-arc tholeiitic rocks. Therefore, the origin of the Khara-Nur harzburgites and dunites should have proceeded in two major stages, including

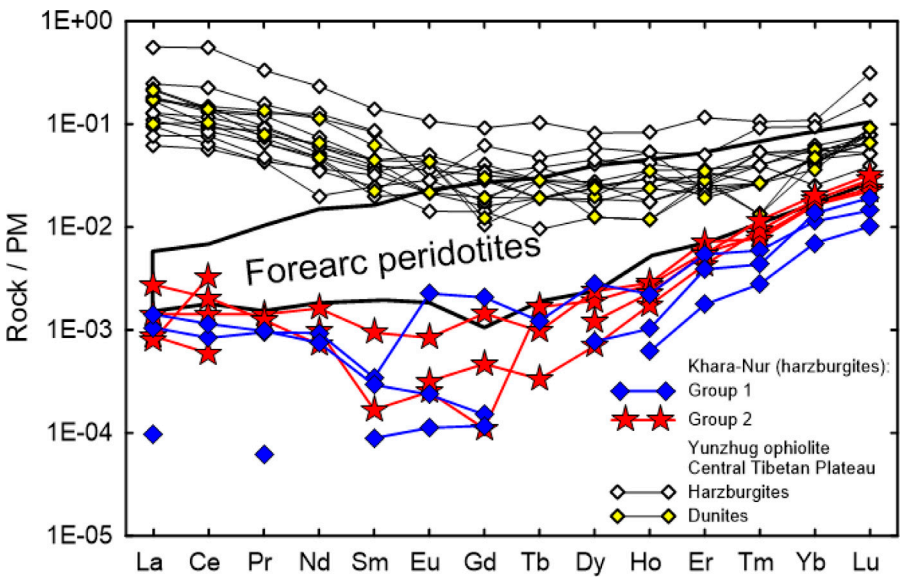

FIGURE 13
PM (Sun and McDonough, 1989) normalized whole rock REE composition of Khara-Nur peridotites. REE composition of peridotites was calculated from mineral modes and REE composition of olivine, orthopyroxene and clinopyroxene (except Cr-Spl, Supplementary Table S1)).

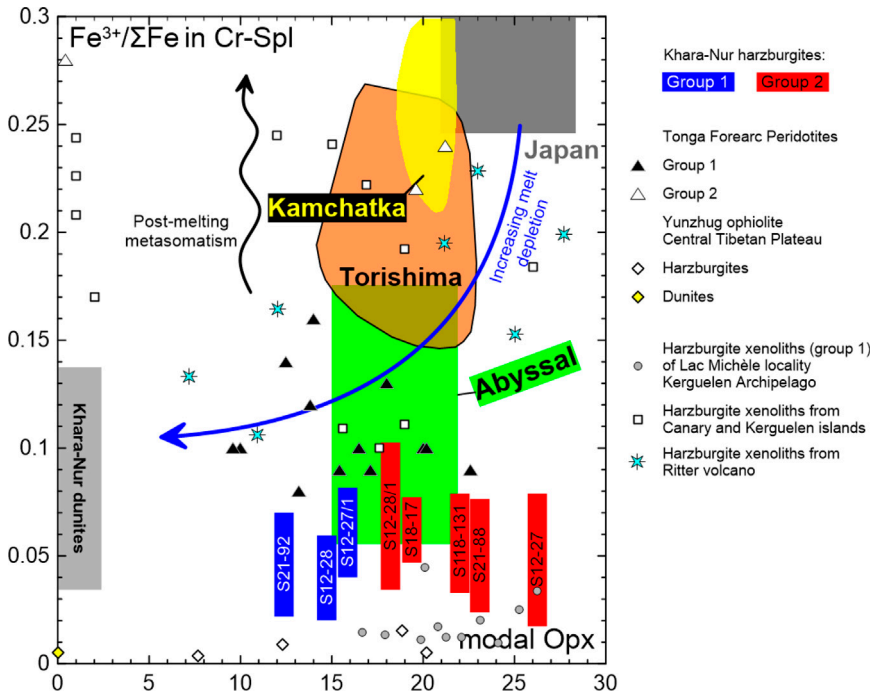

FIGURE 14
Plot of Fe3+/∑Fe in Cr-spinel vs modal orthopyroxene content (in wt%), after (Bénard et al., 2018). Khara-Nur peridotites are shown by blue (group 1) and red (group 2) columns, the values of Fe3+/∑Fe in Cr-spinels are corrected by (Davis et al., 2017) method (see more details in text). Torishima forearc harzburgites and dunites (Parkinson and Pearce, 1998), Tonga forearc peridotites (Birner et al., 2017), harzburgites and dunites of Yunzhug ophiolite (Huang et al., 2020), harzburgite xenoliths (Group 1) of Lac Michele locality of Kerguelen Archipelago (Wasilewski et al., 2017), harzburgite xenoliths from Canary and Kerguelen islands (Neumann et al., 1995; Grégoire et al., 2000), harzburgite xenoliths from Ritter volcano, Bismark arc (Bénard et al., 2017), fields of abyssal peridotites (Dick and Bullen, 1984; Bryndzia and Wood, 1990), spinel harzburgites of Torishima Seamount (Parkinson and Pearce, 1998), harzburgite xenoliths of Avacha volcano, Kamchatka (Ionov, 2010), lherzolite xenoliths from Ichinomegata, Japan (J. Wood and Virgo, 1989) are shown for comparison.

partial melting and further melt-rock interaction, which are considered in detail below.

5.1 Partial melting

The Khara-Nur harzburgites have weakly correlated SiO_2 (42.5–45.0 wt%) and Al_2O_3 (0.48–1.05 wt%) contents, with the latter being a proxy for melting degree (Figure 11). The observed SiO_2—Al_2O_3 systematics allows splitting the mantle rock compositions into two groups (Figure 11B). The Group 1 samples have elevated SiO_2 contents; their compositions variably shift from the compositions of residues from anhydrous melting of fertile lherzolites. Elevated SiO_2 contents are characteristic of arc-related harzburgites (e.g., Parkinson and Pearce, 1998; Song et al., 2009; Birner et al., 2017), which differ from the oceanic harzburgites (Herzberg, 2004). Such peridotites could be residues from hydrous melting of a specific, SiO_2-rich mantle source called "hybrid mantle wedge" (HMW) (Bénard et al., 2017), which forms through enrichment of typical depleted-mantle substrate by slab-derived fluids/melts before or during partial melting. In contrast, the Group 2 harzburgites resemble major-element compositions of residues from anhydrous melting of a source compositionally similar to DM, which was not affected by subduction-zone crust-mantle interactions.

The two groups of Khara-Nur mantle harzburgites and dunites have chemistries consistent with two distinct melting trends (Figure 11B). The modal compositions of harzburgites agree well with calculated amounts of Opx in residues from hydrous and anhydrous melting (Figure 11B; Bénard et al., 2017). For instance, the S12-27 harzburgite contains 26% Opx, which is consistent with the recalculated 23% Opx in a hydrous melting residue. Similarly, for samples S12-27/1 and S12-28 with 15.7% and 15.5% Opx, respectively, predicted Opx in anhydrous melting residue is around 20%. The composition of two dunite samples (S21–89 and S21-78) also tend to follow the mentioned melting trends (Figure 11), and thus have a residual origin. On the contrary, for the rest two dunites, major-element compositions deviate from melting trends and have lower NiO than that of residual dunites (Figures 11B,C,E). The formation of these low-NiO dunites could relate to melt-harzburgite interaction, while fine-grained Cr-Sp and Opx enclosed in Ol of such dunites (Figure 3A) point out Ol crystallization at the expense of Opx both during partial melting and melt-rock interaction.

Based on the whole-rock abundance of Al_2O_3 in residual peridotites, the Khara-Nur harzburgites were produced by ~30–40% melting (Figure 11) in accordance with the lack of residual Cpx in the rocks. Notably, harzburgites of both Groups 1 and 2 have high and similar melting degrees. Within each of the two groups, the samples demonstrate a decrease in modal Opx accompanied by growth in Cr# of Cr-Sp (Figure 12), which is

consistent with partial melting trends. The high melting degrees of both groups of Khara-Nur harzburgites are confirmed by low reconstructed HREE in bulk-rock samples estimated from mineral trace-element abundances and their modal compositions (Figure 13). Similar melting degrees were estimated for typical supra-subduction zone peridotites, including, for instance, the Izu-Bonin-Mariana forearc and Kamchatka arc (within 25%–35%), as well as Bismark arc (to 30%–40%) (Figure 11), whereas the Khara-Nur harzburgites specifically possess calculated HREE values similar to or lower than that of the most depleted forearc peridotites from Izu-Bonin-Mariana (Figure 13).

Alternatively, melting degrees can be estimated from Cr# of Cr-spinel. In case of multi-stage melting started in the garnet-facies and continued in the spinel-facies, Cr-spinel retains Cr# corresponding to a lower melting degree than the bulk melting degree. In both groups of the Khara-Nur harzburgites, the less depleted samples (S12-27 in Group 1 and S12-27/1 in Group 2) preserve Cr-Sp with Cr# of ~0.55 and ~0.56, respectively, which correspond to melting degrees of 18% versus 25%–28% estimated from whole-rock Al_2O_3 abundances. Therefore, two-stage melting scenario should be assumed. The studied harzburgitic Cpx exhibits low MREE/HREE ratios, which are potential indicators of an early-stage, garnet-facies melting episode (Hellebrand, 2002). The estimated equilibrium temperatures for harzburgites obtained from two-pyroxene REE thermometry (862°C–1,093 °C) and Ca-in-Opx and Al-in-Opx thermometry (1,000°C–1,114 °C and 935°C–1,056 °C, respectively) are generally lower than temperatures of melt-harzburgite interaction and magmatic Cpx crystallization (Tollan et al., 2017; Le Roux and Liang, 2019), and should reflect the subsolidus transformation of the rocks. As shown by Liang et al. (2013)and Dygert and Liang (2015), during cooling and subsolidus re-equilibration, REE are redistributed between Opx and Cpx, especially at low Cpx modes and lower temperatures, may also lead to both low MREE/HREE ratios in Cpx. Thus, the trace-element composition of the Khara-Nur Cpx cannot be used unambiguously for modeling of the peridotite partial melting. Nevertheless, the difference in melting degrees estimated from Cr-spinel and whole-rock compositions of Khara-Nur peridotites testifies to the initiation of melting in the garnet-facies.

5.2 Redox state

Previous studies of forearc peridotites documented that their oxygen fugacity values vary from those of mid-ocean ridge mantle to arc xenolith peridotites (Parkinson and Pearce, 1998; Pearce et al., 2000; Dare et al., 2009; Birner et al., 2017), being controlled mainly by a contribution from subducted slabs. Thus, the processes of flux melting and melt metasomatism, which involve slab-derived volatile-rich (most importantly, H_2O and S) fluid of melts should generally yield a more oxidized conditions for supra-subduction zone peridotites (Parkinson and Arculus, 1999). As shown above, the Khara-Nur harzburgites of Group 1 have chemical compositions of supra-subduction peridotites enriched in SiO_2, and therefore should be more oxidized with respect to their chemically depleted counterparts. This, however, contradicts the observations of Cr-Sp with $Fe^{3+}/\sum Fe$ ratios lower relative to typical forearc and supra-subduction samples (Figure 14).

Three different approaches are used for estimating $Fe^{3+}/\sum Fe$ ratios in Cr-Sp, including 1) stoichiometric calculation from EPMA data, 2) direct analysis of $Fe^{3+}/\sum Fe$ ratio by Mössbauer/XANES spectroscopy, and 3) a correction method of combined EPMA analysis of unknowns and a set of standards with the reliably estimated $Fe^{3+}/\sum Fe$ ratios (Davis et al., 2017). On Figure 14 we used the $Fe^{3+}/\sum Fe$ ratios in Cr-Sp, obtained by method 3). The data obtained by methods 1) and 3) are consistent (Supplementary Table S2). This is caused by low uncertainties of stoichiometric calculations for Cr-spinels with low $\sum FeO$ abundances and moderate values of Cr#, as well as determination of minor elements (e.g., V, Zn, Ni) (Quintiliani, 2006; Davis et al., 2017; Jia et al., 2022). The low $Fe^{3+}/\sum Fe$ ratios in Cr-spinel are in agreement with V-Yb systematics (Pearce et al., 2000) of the Khara-Nur peridotites exhibiting lower oxygen fugacity conditions compared to that of forearc peridotites of Torishima seamount (Supplementary Figure S2).

Partial melting of the forearc mantle proceeds in two stages, with the early episode of decompression melting in the asthenosphere, which yields only moderate, MOR-like melting degrees and does not enrich the residue in SiO_2 (e.g., Herzberg, 2004). For the Tonga peridotites (e.g., Birner et al., 2017), this early melting stage is recorded by $Fe^{3+}/\sum Fe$ ratios in Cr-Sp, which are transitional between the Khara-Nur harzburgites and Izu-Bonin-Mariana forearc (Torishima) (Figure 14). The second, major stage of melting assisted by slab-derived fluids and hydrous partial melts produce forearc peridotites with higher melting degrees, SiO_2 enrichment and more oxidized conditions (Parkinson and Pearce, 1998).

The Khara-Nur harzburgites of Group 2 are not enriched in SiO_2 but demonstrate high melting degrees, therefore they did not undergo flux melting. The SiO_2-enriched Khara-Nur harzburgites of Group 1 possess high melting degrees, but their $Fe^{3+}/\sum Fe$ ratios in Cr-Sp are too low to support the flux melting. If the Group 1 harzburgites indeed formed due to flux melting, then some subsequent process must necessarily decrease their $Fe^{3+}/\sum Fe$ ratios in Cr-spinel. One possible explanation for decrease of $Fe^{3+}/\sum Fe$ ratios in Cr-spinel during partial melting was suggested for Bismark arc (Bénard et al., 2018), where some harzburgite xenoliths are SiO_2-enriched (Figure 11B), have high melting degrees (30%–40%; Figure 11A), and are relatively reduced as indicated by Cr-Sp composition (Figure 14). These xenoliths were interpreted as products of two-stage melting: flux melting of spinel harzburgites followed by second-stage adiabatic decompression melting (F~5–8%) of the residues experienced a convective ascent in the mantle wedge (Bénard et al., 2018). Such second-stage melting is not fluid-buffered and preferentially introduces Fe^{3+} into the melt, thus decreasing the estimated $Fe^{3+}/\sum Fe$ ratios (Bénard et al., 2018). However, the driving force of such second-stage melting of the already depleted substrate without a slab-derived flux remains uncertain. Such a model cannot be applied to the studied rocks, since the less depleted harzburgites of Khara-Nur Group 1 (samples S12–27, S21-88) have lower $Fe^{3+}/\sum Fe$ ratio in Cr-spinel as compared to Bismark xenoliths with similar modal orthopyroxene (Figure 14), for which the fisrt stage of flux melting is suggested (Bénard et al., 2018). Alternatively, more reduced subduction-related fluids could be considered. For example, such fluids were assumingly involved into redox melting of supra-subduction peridotites of the Yushigou ophiolite (Tibet) with fO_2 < FMQ, as evidenced by primary methane-bearing fluid inclusions in Ol (Song et al., 2009). It is

unlikely that the methane input and redox-melting is accompanied by rock enrichment in SiO_2. If the abovementioned SiO_2 enrichment of the Khara-Nur Group 1 rocks occurred before their introduction to a subduction zone, then redox melting assisted by moderately reduced fluids would be a plausible mechanism for generating harzburgites of Groups 1 and 2 with high melting degrees and low $Fe^{3+}/\sum Fe$ ratios in Cr-Sp. However, the model of redox melting is not favorable for suprasubduction settings (Foley, 2011).

To resume, the compositions of Group 1 and 2 of Khara-Nur harzburgites cannot be explained by the formation *via* the melting models applied for subduction zones. The Khara-Nur peridotites did not experienced melting in the supra-subduction zone where the Eastern Sayan ophiolites formed.

5.3 The evidence of melt-rock interaction

5.3.1 Melt-harzburgite interaction

The observed textural features of the Khara-Nur harzburgites, such as concave grain boundaries and newly formed small grains of Ol, Cr-Sp and Cpx, are commonly produced by peridotite infiltration by silicate melts (Seyler et al., 2007; Suhr et al., 2008), which implies an Opx-consuming reaction Opx + melt1 → Ol + Cr-Sp + melt2. Petrographic observations of harzburgites testify to Opx dissolution and replacement by Cpx (Figure 3E), which could proceed near the lithosphere-asthenosphere boundary (Suhr et al., 2008). Harzburgitic Opx is enriched in LREE, MREE, HFSE, and some fluid-mobile elements (Cs, Ba, Pb) relative to residual Opx predicted from HREE contents (Figure 9B). Newly formed Cpx in the Khara-Nur harzburgites has major and trace element composition akin to those of forearc peridotites (Figures 8C,D, 10A-B), coupled with low HREE contents. The latter points to low melt/peridotite ratio and HREE contents buffered by the residual peridotite composition (Seyler et al., 2007), and accounts for a preferential control of bulk harzburgite composition by melting processes and pre-melting modification. The abundances of other elements (mainly LREE and some fluid-mobile LILE) are evidently controlled by element diffusion and uptake from a percolating melt (Seyler et al., 2007). The process of melt-peridotite interaction is also highlighted by the distribution of platinum-group elements and Re as well as in Re-Os isotope systematics of Khara-Nur peridotites (Wang et al., 2017).

5.3.2 Melt-dunite interaction

The abundant multiphase inclusions of silicate minerals in Cr-Sp and chromite were reported in podiform chromitites (Xiong et al., 2021), as well as in abyssal (Arai et al., 2022) and supra-subduction (Zhou et al., 2021) peridotites. The origin of such inclusions is generally related to crystallization of melt portions (drops) captured by Cr-spinel during melt-rock interaction. In the Khara-Nur dunites, the inclusions in Cr-Sp were observed only in samples with high Cr_2O_3 abundances (0.85–1.94 wt%) and having both large and small euhedral grains of Cr-Sp. These observations suggest the additional crystalliztion of Cr-Sp from a melt oversaturated with Cr. As Opx and Cpx from inclusions in Cr-Sp differ in Mg# from those in boninite- or IAT-derived cumulate rocks of the Eastern Sayan ophiolites (Figures 8A,C), newly formed Cr-Sp would require melt-Sp re-equilibration rather than direct crystallization from a silicate melt.

The inclusions have variable mineral assemblages (Ol±Opx±Cpx±Amp±Phl) with variable modal amount of phases in a single inclusion and their composition, including REE levels and Pb, Sr, Ti, Zr, Hf behavior (Figure 10D). Trace element features of Cpx is especially diverse and may vary both in two adjacent inclusions in a single Cr-spinel grain, and even in two different Cpx grains from a single inclusion (Figures 10C,D). The revealed variations cannot be derived from fractionation of a single silicate melt, but instead require chemical heterogeneity of a parental melt at a mm-scale and/or diffusion-controlled elemental fractionation near precipitating Cr-Sp grains. As a working scenario, Opx consumption *via* incongruent dissolution during melt-rock interaction leads to coexistence of two distinct locally preserved melts (percolating melt and Opx-derived melt), where elemental transfer is governed by a distance to orthopyroxene and diffusion rate of chemical elements (Arai et al., 2022). The enhanced mobility of LILE and Ca relative to the other elements, as well as easier diffusion of Eu^{2+} relative to other REEs (Behrens and Hahn, 2009; Holycross and Watson, 2016) might be responsible for the observed local trace-element variations, such as LILE anomalies or the presence of Eu maximum and minimum in different clinopyroxene grains within a single inclusion (Figure 10D).

Pyroxenes from inclusions in Cr-Sp resemble Mg# and Al_2O_3 of harzburgitic pyroxenes (Figures 8A,C), and Amp and Phl are also high-Mg# in composition. Therefore, high Mg# values of inclusion phases were likely affected by both high Mg# of parental melts and subsolidus re-equilibration with the host Cr-Sp. Assuming the Opx dissolution effect, high Mg# of inclusion phases could be also caused by high MgO abundance increased through a melt-harzburgite reaction. If this was the case, dunites with inclusion-free Cr-Sp either did not have Opx, or their parental melt was Cr-undersaturated.

5.3.3 The nature of percolating melts

The subduction-related melts responsible for melt-harzburgite interaction and partial/complete Opx consumption should have had high-Mg, H_2O-rich composition stressed by newly formed mineral assemblages and the presence of edenitic amphibole, respectively. Based on direct evidence of the low TiO_2 abundances in host Cr-Sp and inclusion phases, infiltrated melts were also depleted in Ti and some other trace elements. Such melts are common for subduction zones and could have the affinity to boninites and IAT reported in the Eastern Sayan ophiolites (Kuzmichev, 2004; Sklyarov et al., 2016; Belyaev et al., 2017). Most likely, melts involved into harzburgite and dunite metasomatism were compositionally similar and related to the same magmatic pulses, whereas dunites could have been transporting channels for such melts, as suggested for other ophiolite complexes (Zhou et al., 2021).

5.4 The nature of Khara-Nur peridotites: accreted remnants of subcontinental lithospheric mantle?

Most of the provided data favor the origin of the Eastern Sayan ophiolites and—in particular—the Khara-Nur mantle peridotites in a forearc area (Khain et al., 2002; Belyaev et al., 2017, this study). However, multiple petrological and geochemical evidences imply a

protracted history of the parental mantle before its entrainment in a subduction-zone setting: low $Fe^{3+}/\sum Fe$ ratios in Cr-spinel, whole-rock chemical pre-enrichment (e.g., in SiO_2), and also ancient Paleoproterozoic to Mesoproterozoic Re-Os model ages of Khara-Nur peridotites (Wang et al., 2017). The protracted and multi-stage mantle evolution is commonly implied for subduction-zone peridotites based on their Re-Os model age characteristics, which variably pre-date their formation. For instance, the ancient Re depletion ages of ~1.2 Ga for the forearc peridotites from the Torishima seamount (Eocene Izu-Bonin-Mariana forearc) were interpreted to reflect mantle source heterogeneity and an early stage of melting and subduction-driven enrichment before second-stage melting during subduction initiation (Parkinson et al., 1998). Furthermore, similar inferences were made for highly refractory peridotites from modern oceanic lithosphere and oceanic islands (e.g., Simon et al., 2008; Neumann and Simon, 2009; Dijkstra et al., 2010), which have major-element composition similar to that of forearc peridotites (Parkinson and Pearce, 1998) and suprasubduction xenoliths (Ionov, 2010), and exhibit $Fe^{3+}/\sum Fe$ ratios in Cr-Sp similar to that in forearc and supra-subduction peridotites (Figure 14). Simon et al. (2008) and Neumann and Simon (2009) supposed that the highly refractory

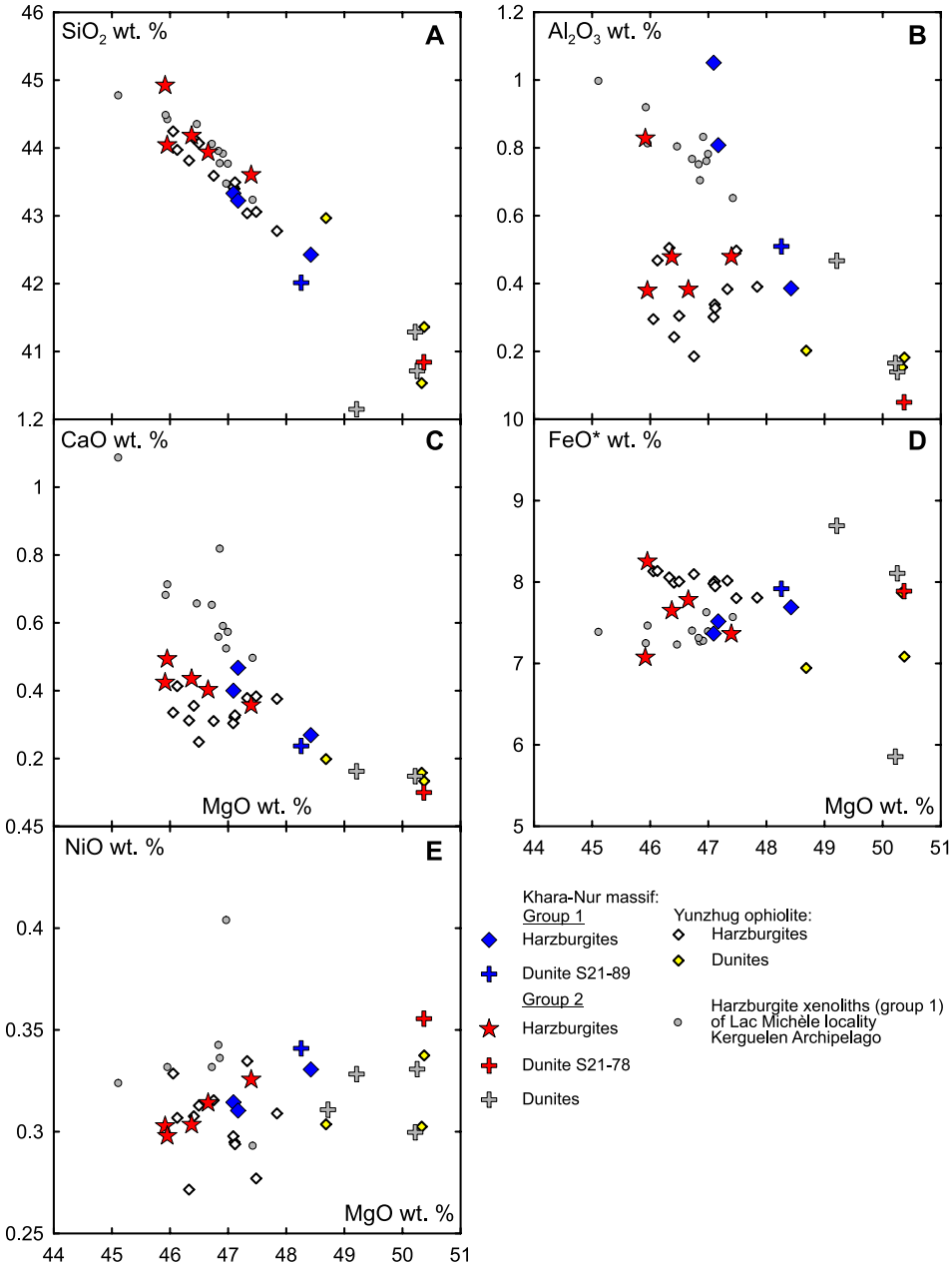

FIGURE 15
Co-variation plots of major oxides vs MgO **(A–E)**. All Khara-Nur peridotite symbols are as in Figure 5. Harzburgites and dunites of Yunzhug ophiolite (Huang et al., 2020) and harzburgite xenoliths of Lac Michèle locality of Kerguelen Archipelago (Wasilewski et al., 2017) are shown for comparison.

peridotites of oceanic islands originate from two-stage melting (MOR-type + flux melting), similar to that of forearc peridotites, and may be accreted to the basement of oceanic lithospheric mantle through the ongoing subduction. This scenario could be viable for the Khara-Nur peridotites if they would not have such low $Fe^{3+}/\sum Fe$ ratios in Cr-Sp.

Alternatively, highly refractory peridotites of oceanic islands could represent the remnants of subcontinental lithospheric mantle. O'Reilly et al. (2009) provided a few lines of evidence that refractory and buoyant ancient cratonic lithospheric mantle blocks could be incorporated into the oceanic mantle during continental rifting and opening of oceanic basins. This would generally explain the ancient Re-Os ages of peridotites and enriched Nd-Sr isotopic signatures of oceanic intraplate basalts (O'Reilly et al., 2009). Such interpretations were favored, for instance, in case of peridotites from Lac Michèle locality of Kerguelen archipelago (Wasilewski et al., 2017) or the Yunzhug ophiolite (Tibet) (Huang et al., 2020), assumed to represent blocks of Proterozoic SCLM. It is known that the Precambrian SCLM (as well as supra-subduction lithosphere) has a specific, SiO_2-enriched composition (Herzberg, 2004). A comparison of Khara-Nur harzburgites with Lac Michèle (Kerguelen) xenoliths (Wasilewski et al., 2017) and Yunzhug peridotites (Huang et al., 2020) demonstrates their similarity in terms of whole-rock major elements (Figure 15), olivine (Figure 6), ortho- and clinopyroxene compositions (Figure 8). Moreover, in Lac Michèle and Yunzhug peridotites the Cr-spinel has very low $Fe^{3+}/\sum Fe$ ratios (Figure 14). Foley (2011) reviewed the available data on peridotites from different tectonic settings and demonstrated that the oceanic and continental (cratonic and off-cratonic) mantle has variably reduced composition (fO_2<FMQ-1). In opposite, the subduction-related peridotite xenoliths are relatively oxidized, with average fO_2 value of FMQ+0.51 and considerable number of samples with fO_2>FMQ+1. In the Khara-Nur harzburgites and dunites, the $Fe^{3+}/\sum Fe$ ratios of Cr-spinel are transitional between those in Cr-spinel from Proterozoic SCLM mantle block in the Yunzhug ophiolite (Huang et al., 2020) and typical forearc (Parkinson and Pearce, 1998) and supra-subduction peridotites (Ionov, 2010). This potentially indicates a transitional composition and redox state of the Khara-Nur peridotites due to melt interaction of the former refractory subcontinental mantle in the mantle wedge (Figure 14).

To resume, the compositional features of the studied Khara-Nur peridotites correspond best to their origin from more ancient Proterozoic mantle with sub-continental lithospheric affinity interacted with supra-subduction melts in a mantle wedge. Boninites and IAT in Eastern Sayan ophiolites formed due to melting of asthenospheric mantle, which experienced upwelling as a result of intra-oceanic subduction initiation. At the same time, the upward flows of the asthenospheric mantle could entrap refractory and buoyant blocks of SCLM incorporated into the oceanic mantle *via* mechanism suggested by O'Reilly et al. (2009) and further transport them in the mantle wedge. Later, the refractory Khara-Nur peridotites were tectonically juxtaposed with the crustal rocks of the Eastern Sayan ophiolite.

6 Conclusion

The Khara-Nur peridotites are represented by highly refractory spinel harzburgites and dunites with major and trace-element whole-rock and mineral compositions resembling forearc and arc peridotites. The two groups are recognized among the Khara-Nur peridotites, which include enriched and not enriched in SiO_2 rocks. The microstructural features, composition of newly-formed minerals (olivine, clinopyroxene, Cr-spinel), the presence of crystallized melt inclusions in Cr-spinel from dunites as well as heterogeneous composition of pyroxenes and amphibole from these inclusions testify to the interaction of the Khara-Nur peridotites with percolating subduction zone-related low-Ti melts. Along with the highly depleted signatures, the Khara-Nur harzburgites demonstrate lower $Fe^{3+}/\sum Fe$ ratios in Cr-spinel than commonly estimated values for typical supra-subduction peridotites, which cannot be explained by existing models of melting above subduction zones. The Khara-Nur harzburgites have whole-rock and mineral compositions resembling those of Proterozoic subcontinental lithospheric mantle peridotites, and demonstrate ancient (Paleoproterozoic to Mesoproterozoic) Re depletion model ages (Wang et al., 2017). We interpret this to be derived from a multi-stage mantle evolution: 1) the formation of Khara-Nur harzburgites and dunites as part of Proterozoic SCLM, resulted in their ultra-depleted affinities and SiO_2 enrichment; 2) incorporation of these SCLM remnants in the supra-subduction zone which produced boninites and island arc tholeiites, preserved now in the crustal part of Eastern Sayan ophiolites; 3) interaction of Khara-Nur peridotites with high-Mg, low-Ti hydrous melts in this supra-subduction zone.

Data availability statement

The original contributions presented in the study are included in the article/Supplementary Material, further inquiries can be directed to the corresponding author.

Author contributions

MG: Conceptualization, Investigation, Supervision, Writing–original draft, Writing–review and editing. VB: Conceptualization, Investigation, Writing–review and editing, Writing–original draft. AK: Conceptualization, Formal Analysis, Investigation, Validation, Visualization, Writing–review and editing. SS: Conceptualization, Funding acquisition, Project administration, Writing–review and editing. NK: Formal Analysis, Methodology, Writing–review and editing. AM: Formal Analysis, Writing–review and editing. NB: Formal Analysis, Writing–review and editing.

Funding

The author(s) declare financial support was received for the research, authorship, and/or publication of this article. The study was funded by a grant from the Russian Science Foundation No. 21-77-10038. https://rscf.ru/en/project/21-77-10038/

Acknowledgments

We thank Dmitri Ionov and Dmitry Kuzmin for providing a set of Cr-spinel samples with $Fe^{3+}/\sum Fe$ ratios measured by Mössbauer spectroscopy, used as secondary standards. We are grateful to Sergei Simakin and Evgeniy Potapov who performed SIMS analyses.

Conflict of interest

The authors declare that the research was conducted in the absence of any commercial or financial relationships that could be construed as a potential conflict of interest.

Publisher's note

All claims expressed in this article are solely those of the authors and do not necessarily represent those of their affiliated organizations, or those of the publisher, the editors and the reviewers. Any product that may be evaluated in this article, or claim that may be made by its manufacturer, is not guaranteed or endorsed by the publisher.

Supplementary material

The Supplementary Material for this article can be found online at: https://www.frontiersin.org/articles/10.3389/feart.2023.1270053/full#supplementary-material

References

Amosova, A. A., Panteeva, S. V., Tatarinov, V. V., Chubarov, V. M., and Finkelstein, A. L. (2015). X-ray fluorescence determination of major rock forming elements in small samples 50 and 110 mg. *Anal. Control* 19, 130–138. doi:10.15826/analitika.2015.19.2.009

Arai, S., and Ishimaru, S. (2007). Insights into petrological characteristics of the lithosphere of mantle wedge beneath arcs through peridotite xenoliths: A review. *J. Petrology* 49, 665–695. doi:10.1093/petrology/egm069

Arai, S., Tamura, A., Miura, M., and Morishita, T. (2022). Origin of spinel-hosted mineral inclusions in mantle peridotite from setogawa in the circum-izu massif serpentine belt, central Japan: implications for the chromitite genesis. *Ore Geol. Rev.* 140, 104422. doi:10.1016/j.oregeorev.2021.104422

Ballhaus, C., Berry, R. F., and Green, D. H. (1991). High pressure experimental calibration of the olivine-orthopyroxene-spinel oxygen geobarometer: implications for the oxidation state of the upper mantle. *Contributions Mineralogy Petrology* 107, 27–40. doi:10.1007/BF00311183

Batanova, V. G., Belousov, I. A., Savelieva, G. N., and Sobolev, A. V. (2011). Consequences of channelized and diffuse melt transport in supra-subduction zone mantle: evidence from the voykar ophiolite (polar urals). *J. Petrology* 52, 2483–2521. doi:10.1093/petrology/egr053

Behrens, H., and Hahn, M. (2009). Trace element diffusion and viscous flow in potassium-rich trachytic and phonolitic melts. *Chem. Geol.* 259, 63–77. doi:10.1016/j.chemgeo.2008.10.014

Belyaev, V. A., Wang, K.-L., Gornova, M. A., Dril', S. I., Karimov, A. A., Medvedev, A.Ya., et al. (2017). Geochemistry and origin of the eastern sayan ophiolites, Tuva-Mongolian microcontinent (southern Siberia). *Geodyn. Tectonophys.* 8, 411–415. doi:10.5800/GT-2017-8-3-0250

Bénard, A., Woodland, A. B., Arculus, R. J., Nebel, O., and McAlpine, S. R. B. (2018). Variation in sub-arc mantle oxygen fugacity during partial melting recorded in refractory peridotite xenoliths from the West Bismarck Arc. *Chem. Geol.* 486, 16–30. doi:10.1016/j.chemgeo.2018.03.004

Bénard, A., Arculus, R. J., Nebel, O., Ionov, D. A., and McAlpine, S. R. B. (2017). Silica-enriched mantle sources of subalkaline picrite-boninite-andesite island arc magmas. *Geochimica Cosmochimica Acta* 199, 287–303. doi:10.1016/j.gca.2016.09.030

Bénard, A., and Ionov, D. A. (2013). Melt– and fluid–rock interaction in supra-subduction lithospheric mantle: evidence from andesite-hosted veined peridotite xenoliths. *J. Petrology* 54, 2339–2378. doi:10.1093/petrology/egt050

Birner, S. K., Warren, J. M., Cottrell, E., Davis, F. A., Kelley, K. A., and Falloon, T. J. (2017). Forearc peridotites from Tonga record heterogeneous oxidation of the mantle following subduction initiation. *J. Petrology* 58, 1755–1780. doi:10.1093/petrology/egx072

Bizimis, M., Salters, V. J. M., and Bonatti, E. (2000). Trace and REE content of clinopyroxenes from supra-subduction zone peridotites. Implications for melting and enrichment processes in island arcs. *Chem. Geol.* 165, 67–85. doi:10.1016/S0009-2541(99)00164-3

Borghini, G., Rampone, E., Zanetti, A., Class, C., Cipriani, A., Hofmann, A. W., et al. (2013). Meter-scale Nd isotopic heterogeneity in pyroxenite-bearing Ligurian peridotites encompasses global-scale upper mantle variability. *Geology* 41, 1055–1058. doi:10.1130/G34438.1

Bottazzi, P., Ottolini, L., Vanucci, R., and Zanetti, A. (1994). "An accurate procedure for the quantification of rare earth elements in silicates," in *Secondary ion mass spectrometry* (Yokohama, Japan: Wiley), 927–930.

Brey, G. P., and Köhler, T. (1990). Geothermobarometry in four-phase lherzolites II. New thermobarometers, and practical assessment of existing thermobarometers. *J. Petrology* 31, 1353–1378. doi:10.1093/petrology/31.6.1353

Bryant, J. A., Yogodzinski, G. M., and Churikova, T. G. (2007). Melt-mantle interactions beneath the Kamchatka arc: evidence from ultramafic xenoliths from shiveluch volcano: sub-arc melt-mantle interactions. *Geochem. Geophys. Geosystems* 8. doi:10.1029/2006GC001443

Bryndzia, L. T., and Wood, B. J. (1990). Oxygen thermobarometry of abyssal spinel peridotites; the redox state and C-O-H volatile composition of the Earth's sub-oceanic upper mantle. *Am. J. Sci.* 290, 1093–1116. doi:10.2475/ajs.290.10.1093

Damdinov, B. B., Zhmodik, S. M., Khubanov, V. B., Mironov, A. G., Travin, A. V., and Damdinova, L. B. (2020). Age and geodynamic conditions of formation for the neoproterozoic gold-bearing granitoids in the eastern sayan. *Geotectonics* 54, 356–365. doi:10.1134/S001685212002003X

Dandar, O., Okamoto, A., Uno, M., and Tsuchiya, N. (2023). Mantle hydration initiated by Ca metasomatism in a subduction zone: an example from the chandman meta-peridotite, western Mongolia. *Lithos* 452–453, 107212. doi:10.1016/j.lithos.2023.107212

Dare, S. A. S., Pearce, J. A., McDonald, I., and Styles, M. T. (2009). Tectonic discrimination of peridotites using fO_2–Cr# and Ga–Ti–Fe^{III} systematics in chrome–spinel. *Chem. Geol.* 261, 199–216. doi:10.1016/j.chemgeo.2008.08.002

Davis, F. A., Cottrell, E., Birner, S. K., Warren, J. M., and Lopez, O. G. (2017). Revisiting the electron microprobe method of spinel-olivine-orthopyroxene oxybarometry applied to spinel peridotitesk. *Am. Mineralogist* 102, 421–435. doi:10.2138/am-2017-5823

Dick, H. J. B., and Bullen, T. (1984). Chromian spinel as a petrogenetic indicator in abyssal and alpine-type peridotites and spatially associated lavas. *Contributions Mineralogy Petrology* 86, 54–76. doi:10.1007/BF00373711

Dijkstra, A. H., Sergeev, D. S., Spandler, C., Pettke, T., Meisel, T., and Cawood, P. A. (2010). Highly refractory peridotites on Macquarie Island and the case for anciently depleted domains in the Earth's mantle. *J. Petrology* 51, 469–493. doi:10.1093/petrology/egp084

Dilek, Y., and Furnes, H. (2011). Ophiolite genesis and global tectonics: geochemical and tectonic fingerprinting of ancient oceanic lithosphere. *Geol. Soc. Am. Bull.* 123, 387–411. doi:10.1130/B30446.1

Dobretsov, N. L., Konnikov, E. G., Medvedev, V. N., and Sklyarov, E. V. (1985). "Ophiolites and olistostromes of eastern sayan," in *Riphean – early paleozoic ophiolites of northern eurasia*, 34–58.

Dygert, N., and Liang, Y. (2015). Temperatures and cooling rates recorded in REE in coexisting pyroxenes in ophiolitic and abyssal peridotites. *Earth Planet. Sci. Lett.* 420, 151–161. doi:10.1016/j.epsl.2015.02.042

Evans, K. A., and Frost, B. R. (2021). Deserpentinization in subduction zones as a source of oxidation in arcs: A reality check. *J. Petrology* 62, egab016. doi:10.1093/petrology/egab016

Foley, S. F. (2011). A reappraisal of redox melting in the Earth's mantle as a function of tectonic setting and time. *J. Petrology* 52, 1363–1391. doi:10.1093/petrology/egq061

Furnes, H., and Safonova, I. (2018). Ophiolites of the central asian orogenic belt: geochemical and petrological characterization and tectonic settings. *Geosci. Front.* 10 (4), 1255–1284. doi:10.1016/j.gsf.2018.12.007

Grégoire, M., Moine, B. N., O'Reilly, S. Y., Cottin, J. Y., and Giret, A. (2000). Trace element residence and partitioning in mantle xenoliths metasomatized by highly alkaline, silicate- and carbonate-rich melts (Kerguelen Islands, Indian Ocean). *J. Petrology* 41, 477–509. doi:10.1093/petrology/41.4.477

Grove, T., Chatterjee, N., Parman, S., and Medard, E. (2006). The influence of H2O on mantle wedge melting. *Earth Planet. Sci. Lett.* 249, 74–89. doi:10.1016/j.epsl.2006.06.043

Hattori, K. H., and Guillot, S. (2007). Geochemical character of serpentinites associated with high-to ultrahigh-pressure metamorphic rocks in the alps, Cuba, and the himalayas: recycling of elements in subduction zones. *Geochem. Geophys. Geosystems* 8, n/a. doi:10.1029/2007GC001594

Hattori, K. H., and Guillot, S. (2003). Volcanic fronts form as a consequence of serpentinite dehydration in the forearc mantle wedge. *Geology* 31, 525. doi:10.1130/0091-7613(2003)031<0525:VFFAAC>2.0.CO;2

Hellebrand, E. (2002). Garnet-field melting and late-stage refertilization in residual abyssal peridotites from the Central Indian Ridge. *J. Petrology* 43, 2305–2338. doi:10.1093/petrology/43.12.2305

Hellebrand, E., Snow, J. E., Mostefaoui, S., and Hoppe, P. (2005). Trace element distribution between orthopyroxene and clinopyroxene in peridotites from the gakkel ridge: A SIMS and NanoSIMS study. *Contributions Mineralogy Petrology* 150, 486–504. doi:10.1007/s00410-005-0036-5

Herzberg, C. (2004). Geodynamic information in peridotite petrology. *J. Petrology* 45, 2507–2530. doi:10.1093/petrology/egh039

Holycross, M. E., and Watson, B. E. (2016). Diffusive fractionation of trace elements in basaltic melt. *Contributions Mineralogy Petrology* 171, 80. doi:10.1007/s00410-016-1289-x

Huang, X.-X., Shi, R.-D., Gong, X.-H., Huang, Q.-S., Griffin, W. L., O'Reilly, S. Y., et al. (2020). Oceanization of the subcontinental lithospheric mantle recorded in the Yunzhug ophiolite, Central Tibetan Plateau. *Lithos* 370–371, 105612. doi:10.1016/j.lithos.2020.105612

Ionov, D. A. (2010). Petrology of mantle wedge lithosphere: new data on supra-subduction zone peridotite xenoliths from the andesitic Avacha volcano, Kamchatka. *J. Petrology* 51, 327–361. doi:10.1093/petrology/egp090

Ionov, D. A., and Wood, B. J. (1992). The oxidation state of subcontinental mantle: oxygen thermobarometry of mantle xenoliths from central asia. *Contributions Mineralogy Petrology* 111, 179–193. doi:10.1007/BF00348950

Ishii, T., Robinson, P. T., Maekava, H., and Fiske, R. (1992). "Petrological studies of peridotites from diapiric serpentinite seamounts in the Izu-Ogasawara-Mariana Forearc, Leg 125," in Proceedings of the ocean drilling program, 125 scientific results *proceedings of the ocean drilling program*. P. Fryer, J. A. Pearce, L. B. Stokking, et al. (Texas, USA: College Station), 445–485. doi:10.2973/odp.proc.sr.125.1992

Jia, L., Chen, Y., Mao, Q., Zheng, D., Yuan, J., Li, X., et al. (2022). *In situ* investigation of the valence states of iron-bearing phases in Chang'E-5 lunar soil using FIB, AES, and TEM-EELS techniques. *At. Spectrosc.* 43. doi:10.46770/AS.2022.002

Johnson, K. T. M., Dick, H. J. B., and Shimizu, N. (1990). Melting in the oceanic upper mantle: an ion microprobe study of diopsides in abyssal peridotites. *J. Geophys. Res.* 95, 2661–2678. doi:10.1029/JB095iB03p02661

Karimov, A. A., Gornova, M. A., Belyaev, V. A., Medvedev, A.Ya., and Bryanskiy, N. V. (2020). Genesis of pyroxenite veins in supra-subduction zone peridotites: evidence from petrography and mineral composition of egiingol massif (northern Mongolia). *China Geol.* 2, 299–313. doi:10.31035/cg2020035

Khain, E. V., Bibikova, E. V., Kröner, A., Zhuravlev, D. Z., Sklyarov, E. V., Fedotova, A. A., et al. (2002). The most ancient ophiolite of the central asian fold belt: U–Pb and Pb–Pb zircon ages for the Dunzhugur complex, eastern sayan, Siberia, and geodynamic implications. *Earth Planet. Sci. Lett.* 199, 311–325. doi:10.1016/S0012-821X(02)00587-3

Khedr, M. Z., and Arai, S. (2010). Hydrous peridotites with Ti-rich chromian spinel as a low-temperature forearc mantle facies: evidence from the happo-one metaperidotites (Japan). *Contributions Mineralogy Petrology* 159, 137–157. doi:10.1007/s00410-009-0420-7

Khedr, M. Z., and Arai, S. (2012). Petrology and geochemistry of prograde deserpentinized peridotites from happo-O'ne, Japan: evidence of element mobility during deserpentinization. *J. Asian Earth Sci.* 43, 150–163. doi:10.1016/j.jseaes.2011.08.017

Khedr, M. Z., Takazawa, E., Hauzenberger, C., Tamura, A., Arai, S., Stern, R. J., et al. (2022). Petrogenesis of arcarc-related serpentinized peridotites (Egypt): insights into neoproterozoic mantle evolution beneath the arabian-nubian shield. *J. Asian Earth Sci.* 226, 105078. doi:10.1016/j.jseaes.2022.105078

Kiseleva, O., Serov, P., Airiyants, E., Travin, A., Belyanin, D., Nharara, B., et al. (2022). Nd-Sr Isotopic study of magmatic rocks and 40Ar/39Ar dating of the mafic dike of the proterozoic Ulan-Sar'dag ophiolite mélange (Southern Siberia, East Sayan, Middle Belt, Russia). *Minerals* 12, 92. doi:10.3390/min12010092

Köhler, T. P., and Brey, G. P. (1990). Calcium exchange between olivine and clinopyroxene calibrated as a geothermobarometer for natural peridotites from 2 to 60 kb with applications. *Geochimica Cosmochimica Acta* 54, 2375–2388. doi:10.1016/0016-7037(90)90226-B

Kröner, A., Kovach, V., Alexeiev, D., Wang, K.-L., Wong, J., Degtyarev, K., et al. (2017). No excessive crustal growth in the central asian orogenic belt: further evidence from field relationships and isotopic data. *Gondwana Res.* 50, 135–166. doi:10.1016/j.gr.2017.04.006

Kuzmichev, A. B., and Larionov, A. N. (2013). Neoproterozoic island arcs in east sayan: duration of magmatism (from U–Pb zircon dating of volcanic clastics). *Russ. Geol. Geophys.* 54, 34–43. doi:10.1016/j.rgg.2012.12.003

Kuzmichev, A. B. (2015). "Neoproterozoic accretion of the Tuva-Mongolian massif, one of the precambrian terranes in the central asian orogenic belt," in *Composition and evolution of central asian orogenic belt: Geology, evolution, tectonics, and models* (Stuttgart: Borntraeger Science Publishers), 66–92.

Kuzmichev, A. B. (2004). *Tectonic history of the Tuva-Mongolian massif: easrly baikalian, late baikalian and early caledonian stages*. Moscow: PROBEL.

Le Roux, V., and Liang, Y. (2019). Ophiolitic pyroxenites record boninite percolation in subduction zone mantle. *Minerals* 9, 565. doi:10.3390/min9090565

Liang, Y., Ji, Z., and Liu, B. (2021). What can we learn from REE abundances in clinopyroxene and orthopyroxene in residual mantle peridotites? *Contributions Mineralogy Petrology* 176, 24. doi:10.1007/s00410-021-01780-x

Liang, Y., Sun, C., and Yao, L. (2013). A REE-in-two-pyroxene thermometer for mafic and ultramafic rocks. *Geochimica Cosmochimica Acta* 102, 246–260. doi:10.1016/j.gca.2012.10.035

Manning, C. (2004). The chemistry of subduction-zone fluids. *Earth Planet. Sci. Lett.* 223, 1–16. doi:10.1016/j.epsl.2004.04.030

McDade, P., Blundy, J. D., and Wood, B. J. (2003). Trace element partitioning between mantle wedge peridotite and hydrous MgO-rich melt. *Am. Mineralogist* 88, 1825–1831. doi:10.2138/am-2003-11-1225

Morishita, T., Dilek, Y., Shallo, M., Tamura, A., and Arai, S. (2011). Insight into the uppermost mantle section of a maturing arc: the eastern mirdita ophiolite, Albania. *Lithos* 124, 215–226. doi:10.1016/j.lithos.2010.10.003

Neumann, E.-R., and Simon, N. S. C. (2009). Ultra-refractory mantle xenoliths from ocean islands: how do they compare to peridotites retrieved from oceanic sub-arc mantle? *Lithos* 107, 1–16. doi:10.1016/j.lithos.2008.06.003

Neumann, E.-R., Wulff-Pedersen, E., Johnsen, K., Andersen, T., and Krogh, E. (1995). Petrogenesis of spinel harzburgite and dunite suite xenoliths from lanzarote, eastern canary islands: implications for the upper mantle. *Lithos* 35, 83–107. doi:10.1016/0024-4937(95)91153-Z

O'Neill, H.St. C., and Wall, V. J. (1987). The olivine - orthopyroxene - spinel oxygen geobarometer, the nickel precipitation curve, and the oxygen fugacity of the Earth's upper mantle. *J. Petrology* 28, 1169–1191. doi:10.1093/petrology/28.6.1169

O'Reilly, S. Y., Zhang, M., Griffin, W. L., Begg, G., and Hronsky, J. (2009). Ultradeep continental roots and their oceanic remnants: A solution to the geochemical mantle reservoir problem? *Lithos* 112, 1043–1054. doi:10.1016/j.lithos.2009.04.028

Pagé, P., Bédard, J. H., Schroetter, J.-M., and Tremblay, A. (2008). Mantle petrology and mineralogy of the thetford mines ophiolite complex. *Lithos* 100, 255–292. doi:10.1016/j.lithos.2007.06.017

Palme, H., and O'Neill, H.St. C. (2014). Cosmochemical estimates of mantle composition. *Treatise Geochem.* 3, 1–39. doi:10.1016/B978-0-08-095975-7.00201-1

Parkinson, I. J., and Arculus, R. J. (1999). The redox state of subduction zones: insights from arc-peridotites. *Chem. Geol.* 160, 409–423. doi:10.1016/S0009-2541(99)00110-2

Parkinson, I. J., Hawkesworth, C. J., and Cohen, A. S. (1998). Ancient mantle in a modern arc: osmium isotopes in izu-bonin-mariana forearc peridotites. *Science* 281, 2011–2013. doi:10.1126/science.281.5385.2011

Parkinson, I. J., Johnson, K. T. M., and Ingram, G. (1992). "Trace element geochemistry of peridotites from the izu-bonin-mariana forearc, leg 125," in Proceedings of the ocean drilling program, 125 scientific results *proceedings of the ocean drilling program*. Editors P. Fryer, J. A. Pearce, and L. B. Stokking (Texas, USA: College Station), 487–506. doi:10.2973/odp.proc.sr.125.1992

Parkinson, I. J., and Pearce, J. A. (1998). Peridotites from the izu–bonin–mariana forearc (ODP leg 125): evidence for mantle melting and melt–mantle interaction in a supra-subduction zone setting. *J. Petrology* 39, 1577–1618. doi:10.1093/petroj/39.9.1577

Pearce, J. A., Barker, P. F., Edwards, S. J., Parkinson, I. J., and Leat, P. T. (2000). Geochemistry and tectonic significance of peridotites from the South Sandwich arc–basin system, South Atlantic. *Contributions Mineralogy Petrology* 139, 36–53. doi:10.1007/s004100050572

Philippot, P., and Selverstone, J. (1991). Trace-element-rich brines in eclogitic veins: implications for fluid composition and transport during subduction. *Contributions Mineralogy Petrology* 106, 417–430. doi:10.1007/BF00321985

Pinus, G. V., and Kolesnik, Yu. N. (1966). *Alpine-type ultramafic rocks of southern Siberia*. Moscow: Nauka.

Quintiliani, M. (2006). Fe^{2+} and Fe^{3+} quantification by different approaches and fO_2 estimation for Albanian Cr-spinels. *Am. Mineralogist* 91, 907–916. doi:10.2138/am.2006.2000

Reagan, M. K., Ishizuka, O., Stern, R. J., Kelley, K. A., Ohara, Y., Blichert-Toft, J., et al. (2010). Fore-arc basalts and subduction initiation in the izu-bonin-mariana system: fore-arc basalts and subduction initiation. *Geochem. Geophys. Geosystems* 11. doi:10.1029/2009GC002871

Ridolfi, F., Renzulli, A., and Puerini, M. (2010). Stability and chemical equilibrium of amphibole in calc-alkaline magmas: an overview, new thermobarometric formulations

and application to subduction-related volcanoes. *Contributions Mineralogy Petrology* 160, 45–66. doi:10.1007/s00410-009-0465-7

Rogkala, A., Petrounias, P., Tsikouras, B., and Hatzipanagiotou, K. (2017). New occurrence of pyroxenites in the veria-naousa ophiolite (north Greece): implications on their origin and petrogenetic evolution. *Geosciences* 7, 92. doi:10.3390/geosciences7040092

Scambelluri, M., Bottazzi, P., Trommsdorff, V., Vannucci, R., Hermann, J., Gòmez-Pugnaire, M. T., et al. (2001). Incompatible element-rich fluids released by antigorite breakdown in deeply subducted mantle. *Earth Planet. Sci. Lett.* 192, 457–470. doi:10.1016/S0012-821X(01)00457-5

Schneider, M. E., and Eggler, D. H. (1986). Fluids in equilibrium with peridotite minerals: implications for mantle metasomatism. *Geochimica Cosmochimica Acta* 50, 711–724. doi:10.1016/0016-7037(86)90347-9

Seyler, M., Brunelli, D., Toplis, M. J., and Mével, C. (2011). Multiscale chemical heterogeneities beneath the eastern southwest Indian ridge (52E68E): trace element compositions of alongaxis dredged peridotites. *Geochem. Geophys. Geosyst.* 12, Q0AC15. doi:10.1029/2011GC003585

Seyler, M., Cannat, M., and Mével, C. (2003). Evidence for major-element heterogeneity in the mantle source of abyssal peridotites from the southwest Indian ridge (52° to 68°E): major-element heterogenity. *Geochem. Geophys. Geosystems* 4, 1–33. doi:10.1029/2002GC000305

Seyler, M., Lorand, J.-P., Dick, H. J. B., and Drouin, M. (2007). Pervasive melt percolation reactions in ultra-depleted refractory harzburgites at the mid-atlantic ridge, 15° 20′N: odp hole 1274A. *Contributions Mineralogy Petrology* 153, 303–319. doi:10.1007/s00410-006-0148-6

Shkolnik, S. I., Belyaev, V. A., Letnikova, E. F., Demonterova, E. I., Bryansky, N. V., Kolesov, K. K., et al. (2023). The Butugol block: A precambrian exotic block in the basement of the Tuva–Mongolian microcontinent (eastern sayan). *Dokl. Earth Sci.* 510, 365–370. doi:10.1134/S1028334X23600330

Simon, N. S. C., Neumann, E.-R., Bonadiman, C., Coltorti, M., Delpech, G., Grégoire, M., et al. (2008). Ultra-refractory domains in the oceanic mantle lithosphere sampled as mantle xenoliths at ocean islands. *J. Petrology* 49, 1223–1251. doi:10.1093/petrology/egn023

Sklyarov, E. V., and Dobretsov, N. L. (1987). Metamorphism of the old ophiolites of the east and west sayan. *Geol. i Geofiz.* 28, 3–14.

Sklyarov, E. V., Kovach, V. P., Kotov, A. B., Kuzmichev, A. B., Lavrenchuk, A. V., Perelyaev, V. I., et al. (2016). Boninites and ophiolites: problems of their relations and petrogenesis of boninites. *Russ. Geol. Geophys.* 57, 127–140. doi:10.1016/j.rgg.2016.01.009

Skopintsev, V. G., Skopintseva, E. V., Ivlev, A. S., Kapitalinina, L. L., Katyukha, Yu. P., and bednenko, N.Yu. (2021). *State geological map of Russian Federation, scale 1:200 000, sheet N-47-XXXV. Explanatory note*. Moscow: Moscow Branch of VSEGEI.

Skuzovatov, S.Yu., Belozerova, O.Yu., Vasil'eva, I. E., Zarubina, O. V., Kaneva, E. V., Sokolnikova, Yu. V., et al. (2022). Centre of isotopic and geochemical research (IGC SB RAS): current state of micro- and macroanalysis. *Geodyn. Tectonophys.* 13. doi:10.5800/GT-2022-13-2-0585

Song, S., Su, L., Niu, Y., Lai, Y., and Zhang, L. (2009). CH_4 inclusions in orogenic harzburgite: evidence for reduced slab fluids and implication for redox melting in mantle wedge. *Geochimica Cosmochimica Acta* 73, 1737–1754. doi:10.1016/j.gca.2008.12.008

Spandler, C., Mavrogenes, J., and Hermann, J. (2007). Experimental constraints on element mobility from subducted sediments using high-P synthetic fluid/melt inclusions. *Chem. Geol.* 239, 228–249. doi:10.1016/j.chemgeo.2006.10.005

Su, B., Chen, Y., Guo, S., and Liu, J. (2016). Origins of orogenic dunites: petrology, geochemistry, and implications. *Gondwana Res.* 29, 41–59. doi:10.1016/j.gr.2015.08.001

Suhr, G., Kelemen, P., and Paulick, H. (2008). Microstructures in hole 1274A peridotites, ODP leg 209, mid-atlantic ridge: tracking the fate of melts percolating in peridotite as the lithosphere is intercepted. *Geochem. Geophys. Geosystems* 9. doi:10.1029/2007GC001726

Sun, C., and Liang, Y. (2014). An assessment of subsolidus re-equilibration on REE distribution among mantle minerals olivine, orthopyroxene, clinopyroxene, and garnet in peridotites. *Chem. Geol.* 372, 80–91. doi:10.1016/j.chemgeo.2014.02.014

Sun, S.-s., and McDonough, W. F. (1989). Chemical and isotopic systematics of oceanic basalts: implications for mantle composition and processes. *Geol. Soc. Lond. Spec. Publ.* 42, 313–345. doi:10.1144/GSL.SP.1989.042.01.19

Suturin, A. N. (1978). *Geochemistry of ultramafic rocks of eastern sayan*. Novosibirsk: Nauka.

Tollan, P. M. E., Dale, C. W., Hermann, J., Davidson, J. P., and Arculus, R. J. (2017). Generation and modification of the mantle wedge and lithosphere beneath the west bismarck island arc: melting, metasomatism and thermal history of peridotite xenoliths from ritter island. *J. Petrology* 58, 1475–1510. doi:10.1093/petrology/egx062

Whattam, S. A., Cho, M., and Smith, I. E. M. (2011). Magmatic peridotites and pyroxenites, andong ultramafic complex, korea: geochemical evidence for supra-subduction zone formation and extensive melt–rock interaction. *Lithos* 127, 599–618. doi:10.1016/j.lithos.2011.06.013

Wang, K.-L., Chu, Z., Gornova, M. A., Dril, S., Belyaev, V. A., Lin, K.-Y., et al. (2017). Depleted SSZ type mantle peridotites in proterozoic eastern sayan ophiolites in Siberia. *Geodyn. Tect.* 8, 583–587. doi:10.5800/GT-2017-8-3-0298

Wang, X., Hou, T., Wang, M., Zhang, C., Zhang, Z., Pan, R., et al. (2021). A new clinopyroxene thermobarometer for mafic to intermediate magmatic systems. *Eur. J. Mineralogy* 33, 621–637. doi:10.5194/ejm-33-621-2021

Wasilewski, B., Doucet, L. S., Moine, B., Beunon, H., Delpech, G., Mattielli, N., et al. (2017). Ultra-refractory mantle within oceanic plateau: petrology of the spinel harzburgites from lac Michèle, kerguelen archipelago. *Lithos* 272–273, 336–349. doi:10.1016/j.lithos.2016.12.010

Widom, E., Kepezhinskas, P., and Defant, M. (2003). The nature of metasomatism in the sub-arc mantle wedge: evidence from Re–Os isotopes in Kamchatka peridotite xenoliths. *Chem. Geol.* 196, 283–306. doi:10.1016/S0009-2541(02)00417-5

Wood, B. J., and Virgo, D. (1989). Upper mantle oxidation state: ferric iron contents of iherzolite spinels by ^{57}Fe mössbauer spectroscopy and resultant oxygen fugacities. *Geochimica Cosmochimica Acta* 53, 1277–1291. doi:10.1016/0016-7037(89)90062-8

Xie, Z., Hattori, K., Dong, Y., and Wang, J. (2021). *In situ* characterization of forearc serpentinized peridotite from the sulu ultrahigh-pressure terrane: behavior of fluid-mobile elements in continental subduction zone. *Geosci. Front.* 12, 101139. doi:10.1016/j.gsf.2021.101139

Xiong, F., Zoheir, B., Wirth, R., Milushi, I., Qiu, T., and Yang, J. (2021). Mineralogical and isotopic peculiarities of high-Cr chromitites: implications for a mantle convection genesis of the bulqiza ophiolite. *Lithos* 398–399, 106305. doi:10.1016/j.lithos.2021.106305

Yang, G. X., Li, Y. J., Tong, L. L., Wang, Z. P., Si, G. H., Lindagato, P., et al. (2022). Natural observations of subduction initiation: implications for the geodynamic evolution of the paleo-asian ocean. *Geosystems Geoenvironment* 1, 100009. doi:10.1016/j.geogeo.2021.10.004

Zhou, X., Zheng, J., Li, Y., Zhu, H., Griffin, W. L., and O'Reilly, S. Y. (2021). Melt migration and interaction in a dunite channel system within oceanic forearc mantle: the Yushigou harzburgite-dunite associations, north qilian ophiolite (NW China). *J. Petrology* 62, egaa115. doi:10.1093/petrology/egaa115